Electronic defects in metal oxide photocatalysts

Ernest Pastor[1]✉, *Michael Sachs*[2], *Shababa Selim*[2], *James R. Durrant*[2], *Artem A. Bakulin*[2] *and Aron Walsh*[3,4]✉

Abstract | A deep understanding of defects is essential for the optimization of materials for solar energy conversion. This is particularly true for metal oxide photo(electro)catalysts, which typically feature high concentrations of charged point defects that are electronically active. In photovoltaic materials, except for selected dopants, defects are considered detrimental and should be eliminated to minimize charge recombination. However, photocatalysis is a more complex process in which defects can have an active role, such as in stabilizing charge separation and in mediating rate-limiting catalytic steps. In this Review, we examine the behaviour of electronic defects in metal oxides, paying special attention to the principles that underpin the formation and function of trapped charges in the form of polarons. We focus on how defects alter the electronic structure of metal oxides, statically or transiently upon illumination, and discuss the implications of such changes in light-driven catalytic reactions. Finally, we compare oxide defect chemistry with that of new photocatalysts based on carbon nitrides, polymers and metal halide perovskites.

Solid-state photo(electro)chemistry uses semiconductors to capture sunlight and drive useful chemical reactions, such as the production of H_2 from water or the reduction of CO_2 into compounds with a higher energy density such as ethanol. Great progress has been made since the pioneering work by Gerischer on semiconductor–liquid interfaces[1] and the milestone report of water splitting in TiO_2 by Fujishima and Honda[2], making today's semiconductor photo(electro)chemistry an increasingly viable technology. The advances have been such that current research is no longer focused on merely demonstrating catalysis but is aiming to push conversion efficiencies into an economically competitive range and develop working devices[3–6].

The biggest strides in the field have been driven by improvements of well known metal oxides, most notably through nanostructuring (for example, 'cauliflower' α-Fe_2O_3)[7], the assembly of heterojunctions (such as WO_3:$BiVO_4$)[8] and the discovery of more efficient compositions (for example, $SrTiO_3$:Al nanoparticles)[9]. Crucially, all of these advances have been underpinned by improvements in the control of the concentration and distribution of defects, which — even in small amounts — can drastically change the properties of a solid and the performance of a device.

Defects are responsible for various phenomena detrimental to the electronic properties of energy conversion materials. For example, the structural deformations induced by defects can hinder charge transport and the electronic deformations can act as recombination centres that compromise device performance[10] (such as quenched luminescence in Co-doped ZnO). However, despite their name, defects can also have a desirable influence on the material properties. For example, chemical doping can turn an insulating oxide into an efficient photocatalyst by increasing carrier concentrations (for example, doping TiO_2 with Nb increases the electron concentration)[11], concomitantly generating ionized dopants as point defects in the structure. Similarly, control of electronic states associated with defects can help to tune and extend charge-carrier lifetimes[12,13]. Over recent years, there has been increasing awareness of the importance of polarons — namely charges that are trapped through lattice deformations even in the absence of a physical point defect — in the operation of photo(electro)catalytic devices[14,15].

Understanding the role of defects and of localized polaronic charge carriers is helpful for improving functional solids for a broad range of applications, but is imperative in the case of heterogeneous photocatalysts. In such systems, light triggers the reorganization of chemical bonds at a solid–liquid (or sometimes solid–gas) interface, requiring the participation of surface dangling bonds (that is, surface defects) for operation. Even more importantly, defect formation is in itself a chemical reaction that depends strongly on the chemical nature

[1]*ICFO (Institut de Ciències Fotòniques), The Barcelona Institute of Science and Technology, Castelldefels, Spain.*

[2]*Department of Chemistry and Centre for Processable Electronics, Imperial College London, London, UK.*

[3]*Department of Materials, Imperial College London, London, UK.*

[4]*Department of Material Science and Engineering, Yonsei University, Seoul, Korea.*

✉*e-mail: ernest.pastor@icfo.eu; a.walsh@imperial.ac.uk*

https://doi.org/10.1038/s41578-022-00433-0

of the solid. Complications emerge when the materials properties required to favour a desired chemical transformation are not notably different from those that favour defect formation.

In this Review, we discuss the impact that electronic defects have on the function of photo(electro)catalytic oxides. We use the term 'photocatalysis' to refer to both photocatalytic and photoelectrocatalytic processes. Although the operation principles are different in these two cases (BOX 1), herein we emphasize the common role that defects have in such technologies. By electronic defects, we refer to changes in the electronic structure induced by point defects (such as oxygen vacancies) and/or polaronic states associated with charge carriers. Although oxide photocatalysis is an extremely rich field in which promising materials are rapidly being discovered[4,16–26] and new reactions are being catalysed (such as pollutant degradation and the reduction of CO_2)[27–30] both in the liquid and gas phases[31–33], we focus primarily on established cases of photocatalytic oxides used for water splitting. In particular, we use α-Fe_2O_3 (REFS[34–37]), TiO_2 (REFS[38–40]), WO_3 (REFS[41–43]) and $BiVO_4$ (REFS[5,44–46]) as examples to provide a framework within which to understand how defect control can help increase photocatalytic yields in oxide-based systems.

We start by reviewing the defect chemistry in metal oxides, focusing on the formation of structural imperfections in the form of vacancies and polarons, and show how such processes alter the fundamental electronic structure of the catalysts. We then outline the key processes that light-driven catalysts must overcome to realize efficient photocatalysis, from the initial equilibration with the liquid phase to product formation. Next, we discuss how chemical imperfections affect such processes and emphasize how sub-bandgap energy levels affect the optoelectronic properties of the metal oxide and the kinetics and energetics of the reactive excited state. Finally, we compare the defect chemistry in oxides with that of emerging photocatalysts based on carbon nitrides, conjugated polymers and metal halide perovskites, and consider how the lessons learned from these systems can be applied to metal oxide systems.

Point defects in metal oxides

The formation of defects in solids is unavoidable and results in the loss of the translational symmetry of the crystallographic unit cell. Symmetry breaking can happen across multiple dimensions, giving rise to 3D volumetric defects (such as pores), 2D planar defects (such as grain boundaries), 1D linear defects (dislocations) and 0D point defects (such as vacancies)[47,48]. All types of defect can affect the electronic and catalytic properties of metal oxides[49–51], but herein we focus on point defects as they are the most intrinsic and have a major role in the optimization of catalytic performance. For a comprehensive overview of the classification of point defects in crystals and associated characterization techniques, we refer readers to the seminal work of Kröger[52]. We first provide an overview of the electronic structure of metal oxides and use it as a framework to discuss the chemical principles that underpin the formation of imperfections (both in the dark and upon illumination).

Electronic structure and bandgaps

The electronic structure and the magnitude of the bandgap of metal oxides is influenced by the crystal symmetry, the ionicity of the metal–oxygen bond and the degree of orbital mixing or hybridization[53,54]. In general, ionic oxides with a large energy difference between the metal and oxygen atomic orbitals tend to exhibit large bandgaps outside the range of solar energy conversion[55]. This is the case for ZnO (3.4 eV), Ga_2O_3 (4.8 eV) and Al_2O_3 (8.8 eV), which have electronic band structures formed by mixing of O 2*p* and metal *s* orbitals. By contrast, transition metal oxides with partially filled valence *d* orbitals, such as α-Fe_2O_3 (2.2 eV) sustain additional bonding interactions that involve the metal *d* and/or *s* orbitals, which lower the bandgap. Often such changes are sufficient to absorb photons in the visible part of the solar spectrum, which makes these metal oxides prime candidates for photocatalysis.

As a first approximation, the electronic structure of most transition metal oxides can be explained from a crystal field perspective in which the oxygen anions are arranged in different geometries around a metal cation. Electrons that occupy the *d* orbitals of the metal centre experience different degrees of repulsion depending on the orbital orientation with respect to the surrounding oxygen anions. In an octahedral geometry (O_h), metal atomic orbitals with t_{2g} symmetry (d_{xy}, d_{yz}, d_{xz}) are stabilized, while atomic orbitals with e_g symmetry ($d^2_{x-y^2}$, d_{z^2}) are destabilized (FIG. 1a). The removal of an oxygen atom from the octahedron, such as due to an oxygen vacancy or dangling bond at the surface, leads to a square pyramidal symmetry (C_{4v}) with a change in the splitting and stabilization of the t_{2g} and e_g orbitals[56,57] (FIG. 1a).

Although crystal field theory provides an initial estimate of the electronic structure, this model does not describe covalent interactions. This extension is achieved with ligand field theory, which considers the overlap and mixing of oxygen 2*p* and metal 3*d* wavefunctions. Within this molecular orbital perspective, in an octahedral ligand field, metal atomic orbitals with t_{2g} symmetry have weak overlap with ligand O 2*p* orbitals and form π-bonding and π*-antibonding molecular orbitals. By contrast, metal atomic orbitals with e_g symmetry strongly interact with oxygen orbitals to form σ-bonding and σ*-antibonding molecular orbitals with mixed metal–oxygen character. The remaining O 2*p* orbitals that do not interact with *d* states form σ_o-non-bonding orbitals with the same energy as the original atomic orbitals. FIGURE 1b shows a molecular orbital diagram for the building blocks of a transition metal oxide. The nature of the frontier orbitals will determine the redox chemistry and tendency for defect formation.

Frontier orbitals

Although it can be straightforward to define a small set of orbitals as the frontier orbitals (highest occupied molecular orbital (HOMO) and lowest unoccupied molecular orbital (LUMO)) in a molecule that are responsible for the chemical reactivity, in a macroscopic crystal, the picture is complicated by crystal momentum and the associated band dispersion in *k*-space. However, we can

Box 1 | **Solid-state photocatalytic approaches**

Solid-state photocatalysis is generally achieved using particulate systems in suspension and films or through photoelectrochemical (PEC) cells[3,242,243] (see the figure). In a particulate system, a single particle drives a complete redox reaction (oxidation and reduction), often with the aid of a co-catalyst. In such systems, catalytic particles are in close proximity, limiting losses from solution resistance and mass transport but also complicating the collection and separation of products. Traditionally, suspension photocatalysis has been performed in 'baggie systems' (see the figure, panel **a**), but this approach is also being implemented in the form of photocatalytic panels in which the particles are immobilized on support panels. In contrast to suspension systems, in PEC cells, the two reactions occur at separate electrodes — oxidation at the (photo)anode and reduction at the (photo)cathode — thereby facilitating product separation and collection (see the figure, panel **b**). There are multiple PEC cell configurations[244,245]; for example, the electrodes can be joined together to form a compact device or they can be physically separated and connected by wires.

Equally, some systems employ semiconductors as both the photocathode and photoanode, whereas other systems employ just one photoelectrode and a second metallic electrode. The latter case requires the semiconductor to generate enough photovoltage to drive the full reaction (oxidation and reduction) or relies on the assistance of an external voltage source, such as a solar cell. It is important to note that, although the eventual goal is to design a complete functional system, the oxidation and reduction reactions are usually studied separately in order to optimize the active materials. This optimization is achieved by using sacrificial donors in suspensions or by voltage-assisted PEC cells that involve the desired photoelectrode and a metallic counter electrode (see the figure, panel **c**). The alignment of the conduction band (CB) and valence band (VB) with the redox potential (*E*) of the species in solution (inset) will dictate whether a reaction is possible. Defect states have a key role in the different steps of the photoelectrocatalytic process. RHE, reversible hydrogen electrode; TOF, turnover frequency; VBM, valence band maximum.

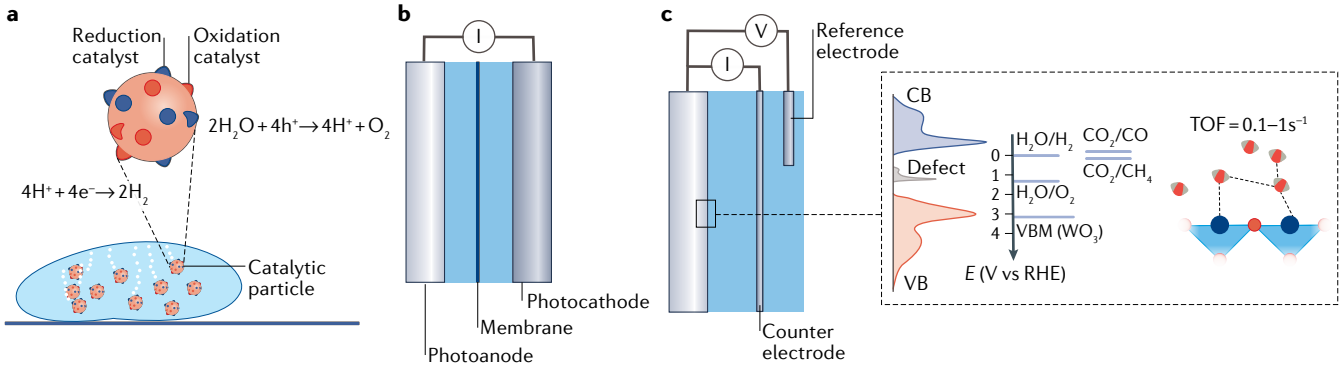

obtain a similar picture by considering groups of bands. Electronic bands are generally grouped as a function of energy and depicted as a density of states (FIG. 1c). The states at the edges — the valence-band maxima (VBM) and conduction-band minima (CBM) — correspond to the frontier crystal orbitals of the metal oxide. The bonding or antibonding nature of those states, as well as their spatial distribution, will dictate the behaviour of the oxide when electrons are added or removed and when dangling bonds are formed either in the bulk or at the surface. Hence, similar to molecular systems, the nature of the VBM and CBM will determine chemical reactivity but also influence the response to defect formation. Indeed, such analysis has been successful in describing physical phenomena in oxides, as well as reactivity trends[58,59].

As a general rule, increasing the electronegativity of the metal cation brings the valence *d* states energetically closer to the O 2*p* states and increases the oxygen–metal hybridization. If the metal valence orbitals are similar in energy to the O 2*p* states, then the upper valence band will be a filled antibonding state, as found for the d^{10} case of Cu_2O (REF.[60]). For the transition metal oxides used in photocatalysis, such as WO_3, $BiVO_3$ and α-Fe_2O_3, the CBM is primarily composed of antibonding metal-like *d* orbitals, whereas the VBM typically consists of a hybridization of metal *d* states with oxygen 2*p* orbitals of bonding character, or non-bonding states[61]. Such an energetic profile has important consequences for the tendency of the metal oxide to form point defects, localize charge in the form of polarons and — ultimately — for the photocatalytic yields. For example, the d^0 conduction band of TiO_2 will become occupied by excess electrons, which can form localized or delocalized charges depending on the crystal polymorph[62].

Types of point defects

Points defects can be broadly classed into two types: first, intrinsic species such as vacancies, when an atom is missing from a regular crystal site, or interstitials, when an atom occupies a crystal site that is normally empty (FIG. 1d); or second, extrinsic species, including the unintentional incorporation of impurities or deliberate doping[63]. As discussed below, trapped electrons in the form of polarons can also be considered a distinct type of electronic defect.

Concentration of point defects

A thermodynamic analysis can yield insight into the concentrations of particular defect species that we might expect in a crystal. The configurational entropy (ΔS) of a static perfect crystal is zero, as each atom is located in its ideal crystallographic site. The consequence is that at non-zero temperatures, the free energy of a crystal ($\Delta G = \Delta H - T\Delta S$, where ΔH is the enthalpy and T is temperature) can be decreased by introducing configurational entropy in the form of defects[47]. A balance emerges between the enthalpic cost of breaking chemical bonds and the entropic gain of forming more imperfections. The resulting exponential dependence means

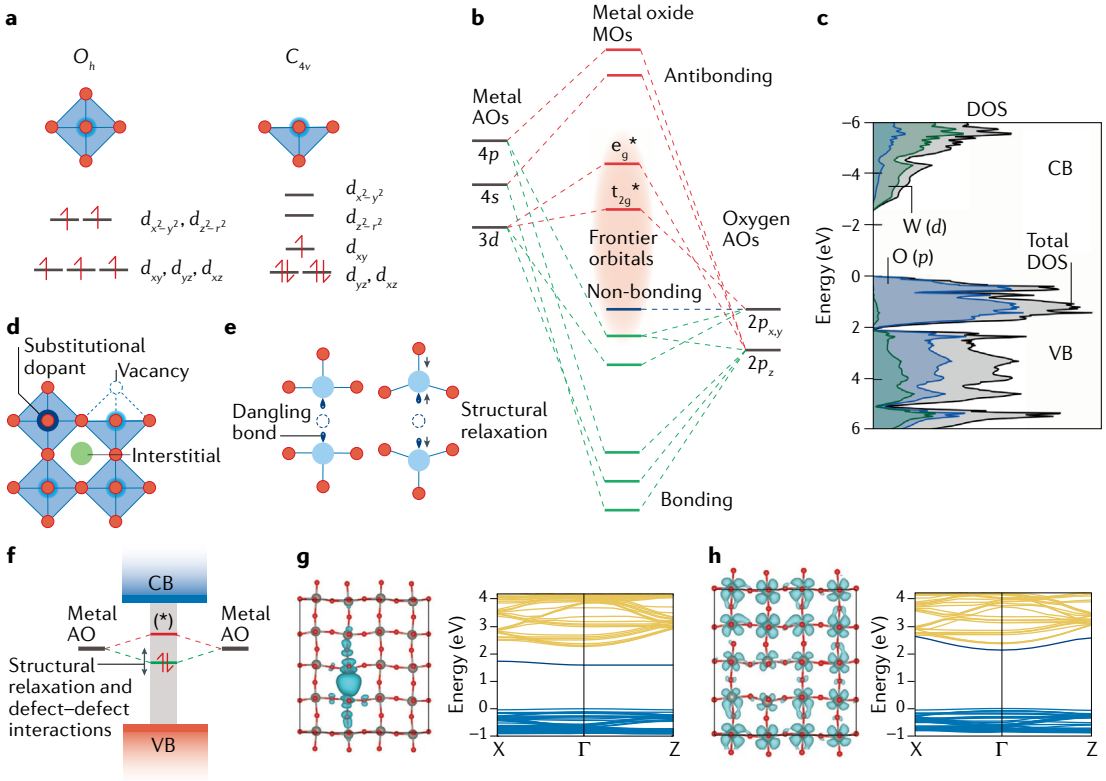

Fig. 1 | **Point defects in a metal oxide. a** | Crystal field splitting of *d* electrons in an octahedral (O_h) and square pyramidal (C_{4v}) coordination environment. **b** | Molecular orbital (MO) diagram describing the building blocks of a transition metal oxide. **c** | Calculated electronic density of states (DOS) of WO_3. **d** | Types of point defects that form in metal oxides. **e** | Oxygen vacancy in an oxide for which the loss of a dangling bond upon ionization results in a structural relaxation. **f** | Electronic band diagram of an oxygen vacancy in a metal oxide. The defect level is close in energy to that of the metal atomic orbitals (AOs) and can be shifted by structural relaxations, as well as defect–defect interactions. **g** | Charge density of a deep vacancy state (left) and the corresponding band structure (right). **h** | Charge density of a shallow vacancy state (left) and corresponding band structure (right). Relaxation of the local structure around the vacancy can induce a transition from a localized (deep) to a delocalized (shallow) state. CB, conduction band; VB, valence band. Panels **g** and **h** adapted with permission from REF.[75], Royal Society of Chemistry.

that the equilibrium concentration (c) of a defect species is highly sensitive to its energy of formation (ΔH_f)[63,64]:

$$c = N\exp\left(-\frac{\Delta H_f}{k_B T}\right) \quad (1)$$

where N represents the density of associated atomic sites in the crystal and k_B is the Boltzmann constant.

What makes the situation more complex is that the defect formation energy is not a constant, but is a function of the atomic and electronic chemical potentials. In this way, the concentrations of different defect species are coupled and the defect profile of a particular sample will depend on its history, including the growth environment (such as the oxygen partial pressure) and thermal processing (such as the annealing time or quenching rate)[65–67]. Let us take the example of the oxygen vacancy — a ubiquitous defect species in metal oxides. Vacancies can be formed by exchange of oxygen with the atmosphere, as described by $O_O \rightleftharpoons V_O + \frac{1}{2}O_{2\,(g)}$. Each oxygen vacancy ($V_O$) has the potential to be a double donor (V_O^{2+}) that will transfer two electrons to the conduction band (n-type donor)[68–70]. The formation energy and equilibrium concentration of this defect will be sensitive to the annealing temperature, the partial pressure of oxygen, as well as the presence of other electron-donating defects in the host crystal. Raising the partial pressure during high-temperature annealing and the presence of an electron-rich environment (n-type) will increase the formation energy and thus decrease the concentration of oxygen vacancies in the bulk. The semiconductor α-Fe_2O_3 has a concentration of oxygen sites in the crystal of ~6×10^{22} cm^{-3}. Assuming a typical defect formation energy of 1 eV, an annealing temperature of 873 K will yield a moderate net vacancy concentration of 6×10^{17} cm^{-3}.

Energy levels in the bandgap

From an electronic viewpoint, the biggest consequence of defect formation is a change in the electroneutrality conditions of the metal oxide. An ideal stoichiometric material has a filled valence band and an empty conduction band, which are separated by a bandgap sufficiently large to suppress thermal excitations of electron and hole charge carriers. The incorporation of charged defects is associated with the creation of new energy levels in the bandgap. The position of sub-bandgap defect levels is related to the energy required to exchange charge

carriers (electrons or holes) with the valence and conduction bands. For example, a singly charged oxygen vacancy (V_O^+) can be further ionized to inject an electron into the conduction band:

$$V_O^+ \rightarrow V_O^{2+} + e^- \quad (2)$$

or it can arrive in the same final charge state by capturing a hole from the valence band:

$$V_O^+ + h^+ \rightarrow V_O^{2+} \quad (3)$$

The energy required for each ionization (ΔE) corresponds to the separation between the defect level and the valence or conduction band edge of the crystal. The location of ionization levels in a semiconductor bandgap is of major interest for the optimization of energy conversion systems because it determines the beneficial or detrimental role of the defect. We distinguish two cases: shallow and deep states. A shallow state describes the case when a defect level lies close (usually within $k_B T \approx 26$ meV at room temperature) to the band edge and can be thermally ionized. A shallow state is often associated with a defect wavefunction that is delocalized over tens to thousands of unit cells[71]. In the hydrogenic limit, for a charged defect in a dielectric host, the shallow state energy is determined by the effective mass ($m^\star$) and the dielectric constant (ε) of the host (in atomic units):

$$\Delta E = \frac{m^\star}{2\varepsilon^2} \quad (4)$$

ΔE values of 1–50 meV are common in tetrahedral semiconductors such as Si and ZnO (REF.[71]). As a consequence, shallow states typically support doping by increasing the concentrations of free carriers in the bands and, thus, the electrical conductivity.

By contrast, a deep state refers to the case when the ionization energy is larger than the thermal energy and is often associated with spatially localized defect wavefunctions on one or a small group of atoms. Deep states are usually formed following a large chemical perturbation, such as a physical vacancy in the structure or an elemental substitution with a large size or orbital mismatch (for example, replacing O by As in a metal oxide). Deep states are often associated with large structural distortions. In optoelectronic and photocatalytic devices, deep states can act as centres for trapping or the recombination of charge carriers and can also pin the Fermi level to a limited energy range inside the bandgap, as discussed below.

We can make a further distinction concerning the defect levels. Optical levels correspond to a rapid vertical excitation (that is, subject to the Franck–Condon principle), during which there is no change in the final defect geometry. By contrast, thermal levels correspond to a slower process, during which the defect geometry has time to transform, as probed using capacitance techniques such as deep-level transient spectroscopy[72]. Therefore, optical levels are deeper than the corresponding thermal levels by an amount that corresponds to the structural relaxation energy of the particular defect species.

From a chemical viewpoint, the depth of the defect states in the bandgap can be understood in terms of the frontier orbitals of the host crystal and the coordination environment of the defect site. The formation of, for example, an oxygen vacancy will create a void with dangling bonds on the adjacent metals that, to a first approximation, will have an energy similar to that of the metal atomic orbitals (FIG. 1e,f). Consequently, the formation of shallow defect states will be favoured when the associated orbitals are located energetically close to the edge of the bands or even within the bands[73]. In addition, weak hybridization between the dangling metals, owing to a large metal–metal distance that reduces orbital overlap and a low coordination environment at the defect site, will favour shallow defect formation[74].

FIGURE 1f exemplifies the formation of new levels in the bandgap owing to vacancy formation. For example, in WO_3, the generation of an oxygen vacancy results in two dangling W bonds with an additional electron each (that is, reduction of W(VI) to W(V)). This configuration leads to the formation of a doubly occupied energy level deep in the bandgap. However, the relaxation of bond lengths around the vacancy to minimize Coulomb repulsion increases the W–W distance and pushes the defect level closer to the conduction band and facilitates the injection of carriers. FIGURE 1g shows a case in which charge is localized around the vacancy and a deep level is formed. In the absence of a strong structural distortion, the charge delocalizes across neighbouring sites, concomitantly forming a shallow defect level[75] (FIG. 1h). When the continuum of states and the wavefunction of the defect overlap, the defect is considered to be resonant with the band[64].

Polarons

An important consequence of point defect formation is the introduction of excess charge (electrons or holes) into a crystal. For example, doping α-Fe_2O_3 with Ti or Sn (REF.[76]), and $BiVO_4$ with W (REF.[77]), increases the concentration of electrons in the host material and enhances its n-type character. Although defects can induce structural relaxations to accommodate the introduction of the dopant atoms, the excess electronic charge can also induce its own lattice distortion[78,79]. In particular, if the solid displays a strong dielectric response (that is, it is highly polarizable), the excess charges (electron or holes) can lower their energy by displacing the surrounding atoms through electron–phonon interactions, forming a quasi-particle known as a polaron[78–83]. As with other point defects, a polaron introduces an energy level in the bandgap (FIG. 2a,b). If the charge and its structural distortion are strongly bound to another defect (such as a vacancy), the polaron can also modify this defect level[55]. For example, electron polarons in $BiVO_4$ that are localized on V centres change the effective oxidation state from V(V) to V(IV) and increase the V–O bond length by ~0.1 Å (REF.[84]). Attaining such a distortion might require an activation energy (FIG. 2b). In addition, different configurations might exist for polarons near a defect (vacancy)[85] (FIG. 2c), which complicates the characterization of the localized state both in the bulk and at the surface.

From an energetic viewpoint, the driving force behind polaron formation is a balance between the

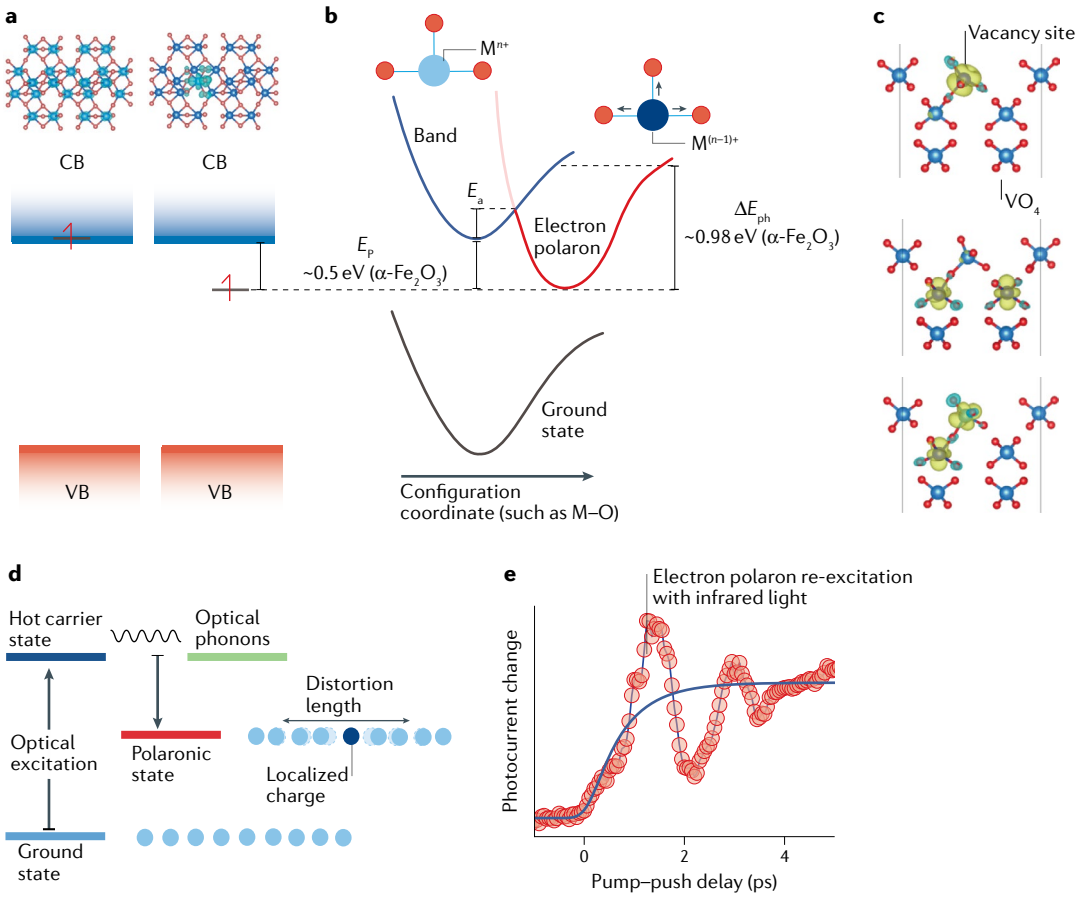

Fig. 2 | **Polaron chemistry. a** | A delocalized conduction-band (CB) electron in α-Fe_2O_3 can localize on an Fe centre, forming a polaronic state and resulting in an energy level in the bandgap. **b** | Configuration coordinate diagram for polaron formation in a metal (M) oxide, displaying the polaron stabilization or binding energy (E_P), the activation barrier for polaron formation (E_a) and the photon energy required to excite the localized state back into the band state with the same atomic configuration (ΔE_{ph}). **c** | Different configurations for small-polaron formation near an oxygen vacancy at the (010) surface of $BiVO_4$. Only the V (dark blue) and O atoms (red) are shown, as well as the spin polarization ($\Delta\rho$; which is the difference in spin-up and spin-down charge densities, with positive $\Delta\rho$ in yellow and negative $\Delta\rho$ in light blue). The top part shows two electrons located at the defect site on a VO_3 polyhedron. The middle part shows an electron on a corner-sharing VO_4 polyhedron and another electron on a separate VO_4 near the surface. The bottom part shows an electron localized on a surface VO_3 polyhedron and an electron on a corner-sharing VO_4 polyhedron. **d** | Steps of photoinduced polaron formation upon bandgap excitation. **e** | Demonstration of ultrafast photoinduced polaron formation. The pump–push photocurrent data shows that when the transient polaronic state is re-excited with infrared light, it causes an increase in device photocurrent. The oscillations are associated with coherent phonon generation. VB, valence band. Panel **c** adapted with permission from REF.[85], American Chemical Society. Panel **e** adapted from REF.[98], CC BY 4.0.

potential energy gain upon distorting the structure and the kinetic energy loss associated with carrier localization[86]. Minimization of the total energy of the additional charge in a dielectric continuum yields the polaron binding energy[86]:

$$E_P = \frac{1}{4\pi^2}\frac{m^* e^4}{2\hbar^2 \varepsilon_{eff}^2} \quad (5)$$

where e is the electronic charge and ε_{eff} is the effective dielectric constant obtained from the static (ε_o) and high-frequency (ε_∞) dielectric constants:

$$\frac{1}{\varepsilon_{eff}} = \frac{1}{\varepsilon_\infty} - \frac{1}{\varepsilon_o} \quad (6)$$

The polaron binding energy refers to the energetic stabilization of a polaronic state with respect to a bare valence-band hole or conduction-band electron. Microscopically, polaron formation is dictated by the coupling between charge carriers and the vibrational degrees of freedom. Within the Landau–Pekar model[87], which considers only the characteristic frequency of a longitudinal optical phonon (ω_o), the strength of this coupling, α_P, is

$$\alpha_F = e^2\left(\frac{1}{\varepsilon_\infty} - \frac{1}{\varepsilon_o}\right)\sqrt{\frac{m^*}{2\omega_o}} \quad (7)$$

Depending on the strength of the electron–phonon coupling, and the extent of the structural distortion, polarons are categorized as large or small[80]. Large polarons (or Fröhlich polarons) exhibit weak coupling and the distortion extends over more than a single unit cell, whereas small polarons (Holstein polarons) are characterized by

strong coupling and distortions that extend over less than a single unit cell with wavefunctions localized to dimensions of the order of interatomic distances.

Polaron formation is favoured in systems with large dielectric constants and heavy effective carrier masses (equations (5) and (7)). Evaluation of the electronic structure can therefore provide an indication of the tendency of a material to form polarons. In general, poor overlap between atomic orbitals will result in weakly dispersive bands and large effective masses for carriers that will favour localization[55]. Metal oxides often fall into this regime, as they have frontier orbitals that are made up of weakly interacting orbitals and a high density of states around the band edges.

Such an electronic structure favourable to polaron formation often occurs in transition metal oxides[55]. Indeed, one of the most studied systems in photocatalysis is TiO_2, which is composed of Ti(IV) $3d^0$ ions and in which electron paramagnetic resonance studies have demonstrated the existence of localized electron states in the form of Ti(III) $3d^1$ ions[88]. Interestingly, in TiO_2, polaron formation depends on the polymorph[83]; in particular, rutile TiO_2 is known to easily form small electron polarons, whereas increasing evidence suggests that anatase TiO_2 sustains large electron polarons[89] characterized by shallow states below the conduction band[90]. Such a difference in polaron formation can explain the distinct behaviours displayed by anatase and rutile in optoelectronic applications[91]. Similarly, polarons have also been reported to affect other oxides used as photocatalysts, electrocatalysts or co-catalysts, including WO_3 (REFS[74,92]), $BiVO_4$ (REFS[84,93–97]), iron oxides[14,98–101], Co_3O_4 (REF.[102]) and titanates[103].

Photoinduced polarons

Light-initiated charge injection into a semiconductor can also trigger the formation of polarons[83,104,105]. Such photoinduced polarons can be formed indirectly through the injection of electrons from a dye molecule on the crystal surface or directly through bandgap excitation and the generation of electron and holes. The mechanism of photoinduced small-polaron formation has been explained with a two-temperature model[14,106]. First, photoexcitation generates a non-thermal distribution of electrons. This hot distribution thermalizes by creating a population of optical phonons. Finally, the electrons and the optical phonons interact to form the small-polaron state (FIG. 2d).

The photoinduced formation of polarons is difficult to track spectroscopically owing to the timescales and length scales involved. This process has been studied using X-ray-based techniques by taking advantage of their elemental sensitivity and the ability to monitor changes in oxidation state upon carrier localization. X-ray absorption spectroscopy monitoring of the Fe K-edge was originally used to detect electron polarons following injection from a molecular dye into Fe(III) (oxyhydr)oxide nanoparticles, albeit with limited time resolution[107]. More recently, polarons produced directly through bandgap excitation of α-Fe_2O_3 were observed using table-top transient extreme-ultraviolet (XUV) spectroscopy on the ultrafast timescale[14,15,99,108–110]. Such studies have revealed that polaron generation depends on the excitation wavelength and, thus, could be related to the wavelength dependence of photocatalytic activity. Moreover, polaron formation in the bulk of an oxide can occur considerably faster than the equivalent process at the surface, indicating that the coordination environment is crucial and that surface polarons can be controlled through materials functionalization[106,111]. X-ray free-electron laser (XFEL) radiation has also been used to track charge-localization processes in TiO_2 (REFS[112,113]); the bright radiation produced by XFELs enables new types of experiments, such as femtosecond resonant inelastic X-ray scattering (RIXS)[114], that can probe charge carriers and structural dynamics in real time and provide new insight into carrier localization.

In addition to X-rays, time-resolved microwave conductivity (TRMC)[115] and terahertz conductivity (TRTC) measurements[96] have been used to identify signatures of polarons in $BiVO_4$. Moreover, ultrafast spectroscopy with photocurrent detection was used to detect small electron polarons in α-Fe_2O_3 photoelectrochemical cells during operation[98]. In this device-based experiment, a 400-nm-laser pump pulse was used to photoexcite an α-Fe_2O_3 photoelectrochemical cell. Subsequently, a second, intense infrared beam directly modulated the polaron sub-bandgap state and transferred the population of localized states into higher-lying energy levels. This re-excitation drove the system through an alternative pathway that increased the cell photocurrent (FIG. 2b,e).

Although the consequences of polaron formation in photocatalysis are discussed in the next sections, recent methodological advances have sparked a renewed interest in polaron chemistry and we refer readers to detailed reviews discussing polaronic effects in inorganic and hybrid materials[83,87,116,117].

Photocatalysis with oxides

Photocatalytic steps

Defects have a key role at each stage of a photocatalytic reaction. The overall reaction can be broken down into five processes (FIG. 3). First, the solid semiconductor and liquid electrolyte phases equilibrate, resulting in the build-up of a semiconductor–liquid junction (FIG. 3a). Second, the absorption of photons with energy greater than that of the bandgap generates charge carriers (electrons and holes) that cool down to the band extrema (FIG. 3b). The third stage involves the separation and transport of the charges from the point of generation to the surface (FIG. 3c). Typical minority carrier diffusion lengths (L_D) are of the order of 5–100 nm in oxides[118]. This distance depends on the carrier mobility (μ) and lifetime (τ) as follows:

$$L_D = \sqrt{\frac{k_B T}{e}\tau\mu} \tag{8}$$

and is therefore very sensitive to charge recombination and localization through defects or polaronic states (FIG. 3d). Finally, charges must be extracted from the semiconductor (FIG. 3e).

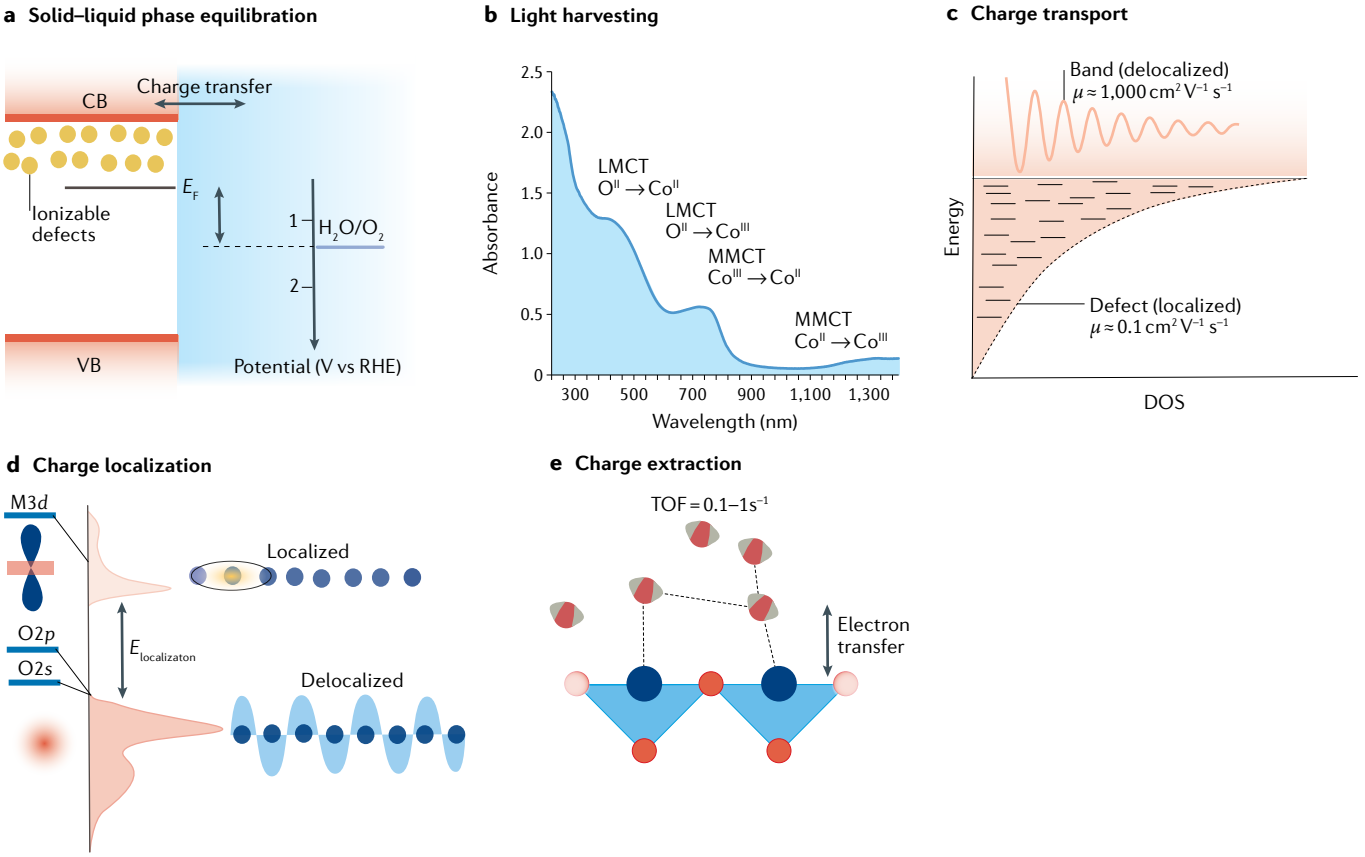

Fig. 3 | **Fundamental steps in photocatalysis. a** | Equilibration between the solid (semiconductor) and liquid (electrolyte) phases. The schematic shows the band positions and thermodynamic reaction energies on the reversible hydrogen electrode (RHE) scale. In the semiconductor (left), ionizable donors act as the primary source of charge. **b** | Absorption of photons for the generation of electrons and holes. Control of the band structure and optical transitions is necessary to maximize absorption in the visible range and ensure the generation of reactive charges. The absorption spectrum shows different types of transitions in Co_3O_4, including ligand-to-metal charge transfer (LMCT) and metal-to-metal charge transfer (MMCT). **c** | Transport of photogenerated charges. Delocalized band states sustain higher carrier mobilities (μ) than do localized states (where DOS is the density of states). **d** | Charge localization in the form of polarons and at physical defects (where $E_{localization}$ is the localization energy). The nature of the frontier orbitals (where M is a transition metal) dictates the tendency to localize charges. **e** | Charge extraction from the semiconductor through a surface chemical transformation. Defects and polarons at the surface alter the energy of reactive intermediates and dictate the accumulation of charge carriers at the active site. Turnover frequencies (TOFs) are typically in the range 0.1–1 s. CB, conduction band; E_F, Fermi level; VB, valence band.

Except for the equilibration with the liquid, all steps are common with other solar energy conversion technologies, such as solar cells. However, the charge-extraction step imposes severe and unique requirements on catalytic materials. From a band structure viewpoint, extraction in a solar cell involves the collection of charges at contact electrodes, whereas the equivalent process in an oxide-based water-splitting device is the four-electron oxidation of water. For such selective chemistry to occur, the frontier orbitals must have the right orbital composition and suitable energetics (that is, in the electrochemical scale, the energy of the VBM must be greater than the redox potential of the species in solution, $E_{VBM} > E^o$(ox/red), for oxidation to occur). From a kinetic viewpoint, charge collection in a solar cell occurs on the nanosecond-to-millisecond timescale[119], whereas water oxidation has been measured to occur on the timescale of seconds, meaning that the photoelectrochemical system requires carriers that are 10^3–10^9 times longer-lived as well as mechanisms for their accumulation near the reaction site[120].

Impact of defects on photocatalysis

Electric field build-up. Semiconductor photocatalysis is enabled by the semiconductor–liquid junction[121]. When the semiconductor is immersed in the electrolyte, charge transfer across the interface takes place until the electrochemical potentials in the solid and the solution are equal, that is, until the Fermi level of the semiconductor (E_F) and the redox potential of the electrolyte (E^o) equilibrate. In the case of an n-type semiconductor with $E_F < E^o$, electrons are transferred to the liquid (FIG. 3a). The larger number of energy states available in the liquid phase means that the energy levels shift mostly within the semiconductor, causing the bands to bend. Through the equilibration process, charged defects play an important part by acting as the source of charge. Beyond the surface atomic layer, charges depleted away from the surface towards the bulk form a depletion region or depletion layer of width W_{SCL} (FIG. 4a). The most important consequence of the equilibration process is the formation of a junction that can assist in charge separation and prevent electron–hole recombination events following

illumination. The strength of the interfacial field can be controlled by changing the density of ionized dopants (N_d), and thus through defect engineering, as well as by applying an external potential. The width of the space charge layer is

$$W_{SCL} = \left(\frac{2\varepsilon\varepsilon_0}{eN_d}\Delta\vartheta\right)^{1/2} \quad (9)$$

where ε and ε_0 are the material and vacuum permittivity, respectively, and $\Delta\vartheta$ is the difference between a given applied potential and the potential at which the bands are flat and there is no excess charge in the semiconductor (termed the flatband potential). FIGURE 4a shows the correlation between the width of the space charge layer and the density of V^{4+} and V^{5+} states associated with oxygen vacancies in $BiVO_4$.

Light absorption. A major approach to lowering the bandgap of photocatalytic oxides and thus enhancing absorption in the visible range is to introduce impurities[4,122]. Doping with metals has been used since the early work on photocatalysis with Cr(III)-doped[123] and V(IV)-doped[124] TiO_2, as well as in studies of $SrTiO_3$ doped with Mn, Ru or Rh (REFS[4,125]). Similarly, the replacement of oxygen atoms with non-metals has been extensively explored, and N-doped TiO_2 and N-doped tantalates are prime examples of materials in which the absorption has been enhanced to reach up to 500–600 nm (REFS[126–128]). Another common strategy

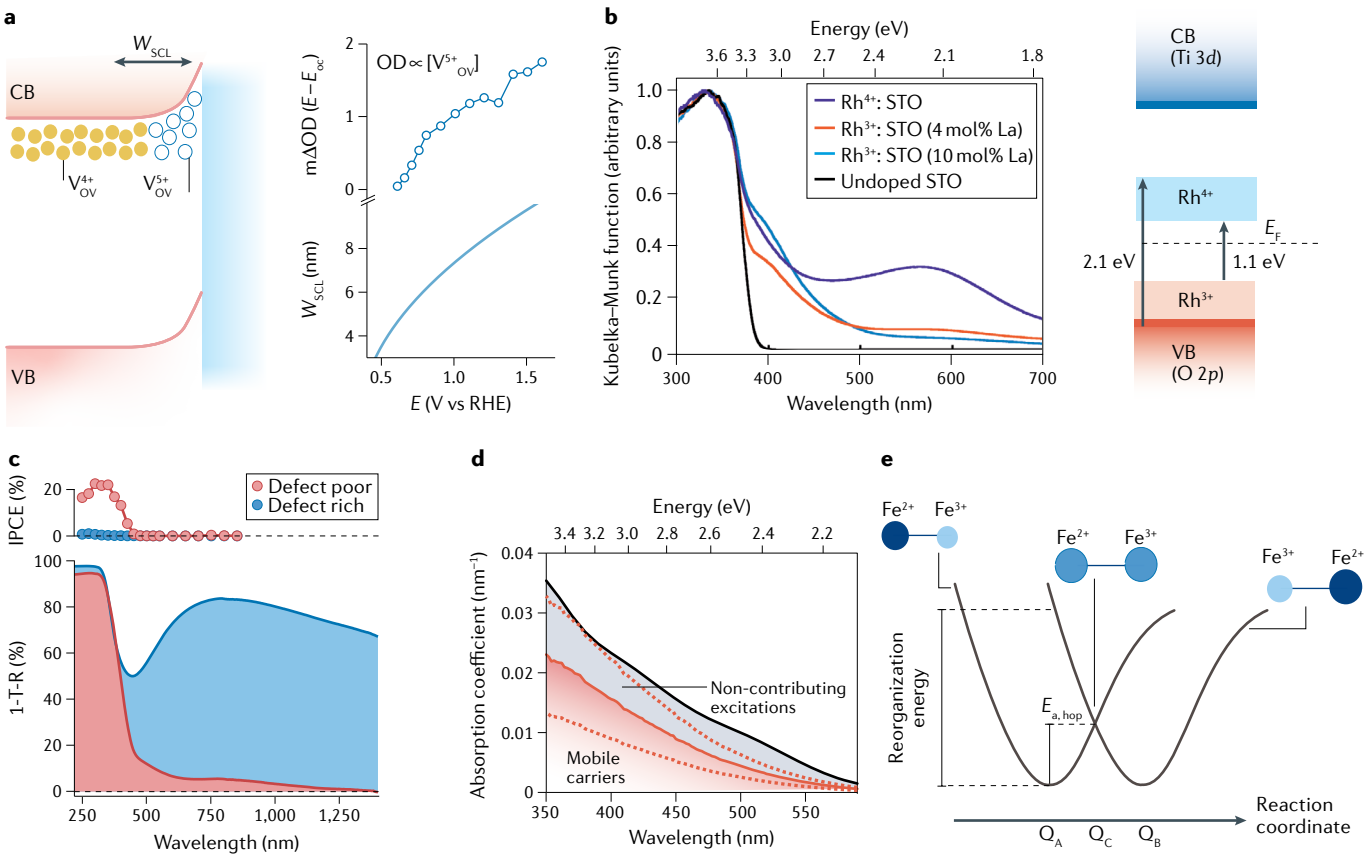

Fig. 4 | **Role of defects in solid–liquid equilibration, light absorption and charge transport. a** | Semiconductor–liquid junction in n-type $BiVO_4$. During equilibration with the electrolyte, filled V^{4+} states associated with oxygen vacancies (OV; orange circles) are emptied (that is, oxidized; empty circles), leading to the formation of a space charge layer of width (W_{SCL}) (left). Positive applied potentials (E) increase the concentration of V^{5+} states and enlarge the space charge layer (right, where ΔOD is the difference in optical density, which is calculated here as the optical signal at each potential minus that at the open-circuit potential (E_{oc})). **b** | Ground-state optical absorption of $SrTiO_3$ (STO) measured in diffuse reflectance mode at different doping densities (left) and the associated band diagram for Rh^{4+}:STO (right). The diagram exemplifies the role of defect engineering in controlling the optical properties of solids. The black trace shows the undoped sample. Doping with Rh^{4+} increases the absorption at long wavelengths (purple). The controlled addition of reduced-valence Rh^{4+} modulates the optical density (orange and blue traces). **c** | Absorption spectra (1-T-R, where R is reflectance and T is transmittance) of defect-poor and defect-rich WO_3. The oxygen vacancies increase the optical density in the visible–near-infrared region; however, light absorption at those wavelengths does not contribute to the water oxidation photocurrent, as shown by the negligible incident-photon-to-current conversion efficiency (IPCE) in this range. **d** | Absorption coefficient of a 7-nm-thick α-Fe_2O_3 thin film (black) compared with the estimated upper and lower (dashed orange lines) and average (solid orange line) proportion of carriers that are active for water oxidation. **e** | Configuration coordinate diagram that exemplifies the principle of electron transfer in the small-polaron regime. The reactants $Fe^{(2+/3+)}$ and products $Fe^{(3+/2+)}$ have equilibrium configurations of Q_A and Q_B, respectively. Electron transfer requires a thermally induced event that excites the sample to an activation energy ($E_{a,hop}$) and brings the system to an intermediate configuration at the crossing point (Q_C). CB, conduction band; VB valence band. Panel **a** adapted with permission from REF.[163], American Chemical Society. Panel **b** adapted with permission from REF.[136], Royal Society of Chemistry. Panel **c** adapted from REF.[74], CC BY 3.0. Panel **d** adapted from REF.[145], Springer Nature Limited.

relies on the formation of oxygen vacancies, which has been used to increase the optical absorption of wide-gap materials, including ZnO (REFS[129,130]), SnO_2 (REF.[131]) and WO_3 (REF.[74]), and even to produce black TiO_2 (REFS[132,133]) and, more recently, black $BiVO_4$ (REF.[134]).

The mechanism by which low dopant concentrations enhance optical absorption is generally the introduction of sub-bandgap states that enable longer-wavelength optical transitions between defect and band states or between the defects themselves. This effect is shown in FIG. 4b for the case of Rh^{4+}-doped $SrTiO_3$, in which the Rh ions substitute the Ti centres[135]. The introduction of Rh^{4+} ions with a $4d^5$ configuration opens up new d–d and charge-transfer transitions that increase the absorption at wavelengths beyond 400 nm (REF.[136]). Further doping with La reduces the valence state of Rh^{4+} through charge compensation, lowering the absorption in the visible region. This sensitivity to the presence of dopants emphasizes that fine control of the intragap density of states is required to modulate the absorption properties on demand. Engineering of the absorption characteristics can be achieved with the principles outlined above. As a first approximation, the defect state will have an energy similar to that of the atomic orbital of origin (for example, the atomic orbital of the cation surrounding an anion vacancy) and the energy level can be tuned by controlling the coordination and bonding of the defect state.

The power of defect control is seen in the case of WO_3, which changes colour from transparent yellow to dark blue with an increase in the density of oxygen vacancies — a property that is exploited for photocatalytic[137,138], photochromic and electrochromic applications[139,140]. When oxygen is released from WO_3 (FIG. 1e), it leaves behind two electrons that localize on two W(VI) centres, reducing them to W(V) (REFS[141,142]). The resulting intragap energy landscape can potentially be composed of deep states associated with the actual vacancy (that is, uncoordinated atomic sites), W $5d^1$ states associated with an electron localized in the vicinity of the vacancy, and W $5d^1$ states caused by an electron and lattice distortion located further away from the vacancy (that is, an electron polaron unbound from the source defect)[143]. The blue colour has primarily been attributed to light absorption of W $5d^1$ centres trapped next to the vacancy (bound polarons) and to the absorption of unbound polaronic states. Both of these processes involve charge transfer between W ions, such as from W(V) to W(VI). The spread of defect levels, and thus the optical transitions available, can be tuned by favouring defect–defect interactions under highly reducing growth conditions. The defect levels for single oxygen vacancies are located up to 0.7 eV below the conduction band, but the formation of defect clusters alters the coordination of the vacancy and its bonding environment. This clustering widens the range of possible charge states and substantially broadens the intragap energy distribution, which can reach as far as 0.9 eV below the conduction band with a concomitant increase in light absorption at long wavelengths[74]. Similar defect–defect interactions are known to have an important role in solar cell materials, such as $Cu(In,Ga)(S,Se)_2$ (REF.[144]), in which they have also been used to control the tolerance to undesired defects. Modulation of defect–defect interactions through control of the concentration and growth environment offers a strategy to tune the density and distribution of intragap states in catalytic oxides.

Although enhancing optical absorption is necessary, it is important to recognize that not all photogenerated charges are ultimately able to drive a desirable photocatalytic reaction. First, charges generated through the direct photoexcitation of defect states, such as oxygen-vacancy absorption bands in highly oxygen-deficient metal oxides, might lack the necessary driving force to perform thermodynamically demanding reactions[74]. For example, for WO_3, the absorption enhancement at ~750 nm due to defect states does not contribute to the water oxidation photocurrent (FIG. 4c). Second, even charges produced by an intrinsic optical transition might not uniformly contribute to catalysis. For example, the average proportion of charges able to drive water oxidation in α-Fe_2O_3 photoelectrochemical cells is substantially smaller than unity (FIG. 4d). Such phenomena have been ascribed to the formation of photoinduced polarons, which, as described below, limit photoconversion efficiencies[145]. The generation of inactive charges is also disproportionately large near the absorption onset, which similarly to observations in early studies, has been attributed to a decreased activity of the ligand field transitions that dominate in the visible spectral range[146–148]. These observations indicate the need to carefully engineer oxides to ensure that light absorption generates excited states (whether band-like or polaronic) that can thermodynamically drive catalysis. Moreover, the strong wavelength dependence of photocatalysis highlights the need to better understand how absorption couples to surface catalysis, as well as the intermediate steps such as charge transport and localization.

Charge transport. One of the main goals for defect engineering of oxide photocatalysts has been to increase the conductivity of majority carriers. For an n-type semiconductor, the electron conductivity (σ) depends on the concentration of electrons (n) and their intrinsic mobilities (μ):

$$\sigma = en\mu \tag{10}$$

Thus, the introduction of high-valence dopants that create shallow defects increases the conductivity by increasing the electron concentration in the conduction band. This effect has been extensively explored; for example, α-Fe_2O_3 has been n-doped with Ti (REFS[149–151]), Si (REF.[7]), Sn (REFS[152,153]) and Ge (REF.[154]), among others, and $BiVO_4$ has been doped with W and Mo, with important implications for their photoelectrochemical performance[155–157]. In addition to metals, the most common source of doping is oxygen vacancies, which are often responsible for the much higher intrinsic doping densities of metal oxides compared with elemental semiconductors[68].

The underlying doping mechanism is not always fully understood, in particular when the excess carriers form polarons. In the small-polaron regime, change transport occurs via hopping between adjacent atomic sites as opposed to band-like transport[83]. This charge transport

mechanism leads to considerably lower carrier mobilities (for example, ~0.1 $cm^2 V^{-1} s^{-1}$ in $BiVO_4$) than in traditional semiconductors (for example, ~1,350 $cm^2 V^{-1} s^{-1}$ for electrons in Si)[158,159]. The reason for such slow transport is that movement of a polaronic charge from site to site requires a structural rearrangement with an activation barrier ($E_{a,hop}$) with the polaron mobility given by $\mu_{pol} \propto e^{-Ea,hop/k_BT}$ (REFS[160,161]). For electron transfer to occur, the reactants must first be excited (for example, thermally) to the activation barrier and assume an intermediate configuration (FIG. 4e). We note that in the diabatic regime, the activation barrier for hopping is related to the polaron binding energy, $E_P \approx 2E_{a,hop}$ (REFS[98,160]) and, thus, the more strongly bound the polaron, the lower its mobility.

$BiVO_4$ is an example of a photocatalyst in which electron transport is considered a limiting factor[162–164]. Although oxygen vacancies are thought to be the source of n-doping, several spectroscopic studies have found that vacancies give rise to donor states as much as 0.6 eV below the conduction band[163,164]. Such deep character should prevent these states from being ionized and, thus, should render them ineffective n-dopants. However, recent theoretical work has explained this discrepancy, suggesting that although the oxygen vacancy states are indeed deep, their ionization to more conductive polaronic states is only of the order of 0.1–0.3 eV (REF.[165]). This vacancy-to-polaron ionization value is consistent with experimentally measured activation energies for carrier de-trapping[163]. Polaron transport is also affected by the differences in the concentration of oxygen vacancies between the bulk and surface, as observed using transmission electron microscopy[166], as well as by variations in the adopted geometrical distortions and configurations[167], all of which can notably alter the mobility and energetics of the respective polarons[85].

In addition to the effects of vacancies, the presence of other imperfections in the crystal can also change polaron transport. For example, doping of α-Fe_2O_3 with Si has been reported to increase the conductivity by increasing carrier concentrations and also by increasing the mobility of small polarons[100]. The incorporation of Si enhanced polaron transport by changing bond lengths, altering hopping probabilities in the system and lowering the activation energy for hopping (FIG. 4e). Crucially, these positive effects of Si are not general for all dopants and might depend on the radius of the foreign atom and the extent to which it distorts the crystal. For example, Sn-doping had a negative effect on polaron mobilities in α-Fe_2O_3, increasing the activation barrier for hopping[152]. However, Sn-doping is used in active α-Fe_2O_3 photoelectrocatalysts because the detrimental effect on polaron transport can be compensated by an increase in electron concentration. These results show that doping is a more complex process than the simple injection of carriers into a band. The countering effects of doping with atoms such as Si and Sn might prove useful in optimizing the carrier density and polaron transport through careful co-doping strategies.

Pump–push photocurrent experiments of α-Fe_2O_3 photoelectrochemical cells have also demonstrated that the formation of electron polarons within less than a picosecond affects charge extraction in the photoelectrochemical device, because there is a large population of polaronic charges that recombine before being extracted[98]. Similarly, ultrafast terahertz conductivity measurements in $BiVO_4$ (REF.[96]) have reported a combined electron–hole peak mobility of 0.4 $cm^2 V^{-1} s^{-1}$ at ~1 ps that decreases by ~70% within the first few hundreds of picoseconds. This loss signifies a substantial loss of free or relatively unbound carriers, which can result from carrier localization. Time-resolved microwave conductivity measurements on the nanosecond-to-millisecond timescale have yielded similar low mobilities for undoped $BiVO_4$, further supporting the localized picture[115]. However, the observed carrier lifetimes of ~40 ns lead to a relatively long calculated carrier diffusion length of ~70 nm and suggest that despite the low mobility, photogenerated charge carriers can access interfaces for reactions in this material.

Impact of charge localization on defects. Even when a beneficial dopant is identified, low doping efficiency is a problem that can affect many oxides. This issue happens when only a small fraction of the dopants is active (ionized). Low doping efficiency can occur either from dopant levels being too deep in the bandgap or the migration of dopants to crystal boundaries, where their behaviour changes and they become inactive.

Deep defect states act as trapping sites for photogenerated charge carriers. Such a trapping process has two main consequences: first, it can immobilize one type of charge carrier through selective trapping and, second, it enables non-radiative electron–hole recombination through a Shockley–Read–Hall mechanism. The first process can be beneficial, because trapped carriers can exhibit very long lifetimes, as observed in different polymorphs of TiO_2 as well as in α-Fe_2O_3 and WO_3 (REFS[120,168–171]). In the absence of other pathways to increase carrier lifetimes, selective trapping can aid charge separation and ultimately improve catalysis.

The complexity of the localization process is exemplified for WO_3 (FIG. 5a). In WO_3, a large part of the W 5*d* vacancy state distribution is energetically too far from the conduction-band edge for thermal excitation[74]. As a consequence, intragap states in WO_3 are largely occupied with electrons (in the form of reduced W(v) centres) and, thus, can act as trapping sites for minority carriers (photogenerated holes). Such trapping enables a relaxation pathway for the hole, through which the energy of the hole is lowered by oxidizing a W(v) centre, losing most of its oxidative driving force in the process. Importantly, hole trapping does not immediately lead to annihilation of the counterpart photogenerated electron. This behaviour is corroborated by measurements on longer timescales, which show a substantial gain in lifetime of up to several milliseconds[74]. Hence, the localization process provides a mechanism by which carrier lifetimes can be extended at the expense of carrier energy or driving force.

The localization process can be tuned by controlling the distribution of intragap defect states and, as expected, highly oxygen-deficient WO_3 with a broad defect distribution exhibits faster trapping than the

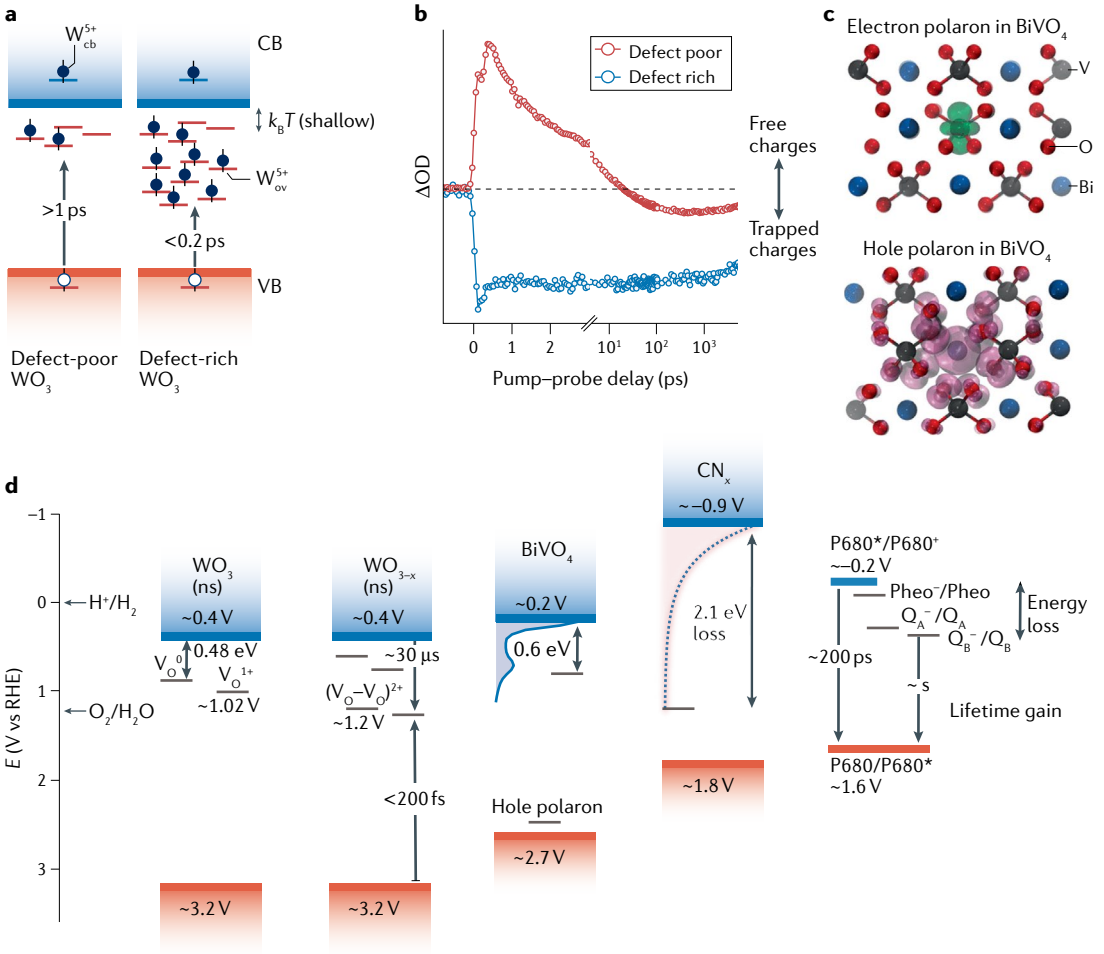

Fig. 5 | **Impact of charge localization on defects and polarons. a** | Band diagram of WO_3. Deep donor states are occupied with electrons (blue circles), providing a pathway for hole (white circles) trapping. **b** | Kinetics of ultrafast hole trapping or localization into W^{5+}_{OV} states associated with oxygen vacancies in WO_3. The negative signals are associated with trapped holes. The localization process is near-instantaneous at high vacancy densities. **c** | Isodensities of the electron and hole polarons in $BiVO_4$. The electron localizes strongly on the V atom, changing the oxidation state from V^{5+} to V^{4+} and increasing the V–O bond length. The hole polaron distributes between the Bi and O atoms, slightly shortening the Bi–O bond. **d** | Intragap defect levels in catalytic oxides, carbon nitride (CN_x) and redox cofactors in photosystem II (where Q_A and Q_B are the primary and secondary plastoquinone electron acceptors, respectively; Pheo is pheophytin; P680 is the chlorophyll that absorbs 680-nm light; and P680* is the excited state of P680) shown relative to the water-splitting thermodynamic potentials[74,84,174,217,241]. The shaded area in $BiVO_4$ corresponds to the distribution of V^{4+}/V^{5+} states obtained from capacitance measurements[163]. In photosystem II, charge separation occurs through a series of redox cofactors, which enable the necessary lifetime gain for water oxidation to take place at the expense of a major energy loss. Similarly, in artificial systems, photogenerated hole trapping into deep defect states increases carrier lifetimes at the expense of a loss in oxidative power. In WO_3, 'ns' indicates near stoichiometric. CB, conduction band; OD, optical density; VB, valence band; V_O, oxygen vacancy. Panel **b** adapted from REF.[74], CC BY 3.0. Panel **c** adapted with permission from REF.[84], American Chemical Society.

near-stoichiometric analogue. This behaviour is exemplified in the transient dynamics of WO_3 (FIG. 5b), in which the appearance of the negative signal is associated with hole trapping[74,171]. The same behaviour has been observed in $BiVO_4$: within <200 fs of photoexcitation, a fraction of the photogenerated holes relax into intragap V(IV) states associated with oxygen vacancies, oxidizing them into V(V) states. Relaxation into such states, which are located at approximately 0.6–0.8 eV relative to the CBM and are thus more negative than the thermodynamic water oxidation potential of 1.23 V versus the reversible hydrogen electrode, renders these photogenerated holes inactive for water oxidation[163].

It is important to note that although a decrease in driving force associated with carrier relaxation means that the charges might become unreactive towards highly demanding, multi-electron reactions, the concomitant increase in lifetime might be advantageous to drive less energetically demanding processes, such as pollutant degradation. Hence, engineering of defect distributions and defect concentrations might open up a route towards tuning oxides to specific catalytic reactions. In this sense, thermodynamically facile reactions might be more tolerant of and even benefit from high defect concentrations, whereas more demanding processes might require lower defect densities. Indeed, the performance

optimum for water oxidation in WO_3 is at only ~2% oxygen vacancies[12].

Impact of charge localization on polarons. The formation of polarons upon photogeneration provides another pathway for carrier energy minimization. In $BiVO_4$, hole polarons are reported to be weakly localized and located only 0.1 eV above the VBM; consequently, polaronic holes can drive water oxidation. By contrast, electron polarons are strongly localized on V atoms and exhibit stabilization energies as large as 0.9 eV relative to the CBM[84] (FIG. 5c). The electron-polaron level is more positive than the H^+/H_2 redox potential, rendering polaronic electrons unreactive towards proton reduction and limiting the ability of $BiVO_4$ to drive the overall water-splitting reaction. Moreover, the electron-polaron level is positioned close to the H_2O/O_2 level, indicating that recombination of electron–hole polarons can effectively compete with charge transfer to the electrolyte[84]. We note that polaron binding energies depend on temperature, the presence of other defects and the physical location within the oxide (that is, surface versus bulk). Consequently, there is a spread of absolute values reported in the literature.

In α-Fe_2O_3, the stabilization energy for electron polarons is also large (~0.5 eV)[98] and decreases the optical gap (2.2 eV) to an effective electronic gap of only ~1.75 eV (REF.[172]). X-ray photoemission studies have suggested that such a large decrease in the energy of the electronic state limits the attainable photovoltage in α-Fe_2O_3 devices and thus restricts its ability to drive photochemical reactions[172]. Similar to what has been observed in other systems such as organic semiconductors, it might be possible to decrease such losses through polaron engineering. One route could be to decrease the binding energy or to increase the activation barrier for polaron formation through crystal engineering (FIG. 2b). This approach would decrease the probability of polaron formation and minimize the decrease in the energy of the electronic state, easing the penalty on the photovoltage. Moreover, a lower polaron binding energy would also induce a lower activation barrier for carrier hopping, increasing transport. Guiding the redesign of polaronic extended solids is non-trivial, but classical concepts derived from coordination chemistry might be of use. Indeed, experiments have shown that photoinduced polaron formation depends on molecular-scale parameters, such as ligand field strength and the metal coordination environment[108]. In this context, strategies such as the use of metal oxyhydroxides or multinary oxide systems such as ferrites, which are being explored for photocatalysis[173], could help control polaron formation and its impact on catalysis.

The band alignment of several frequently used oxides and their respective intragap states are shown in FIG. 5d. Although it has been established that defects affect the performance of these oxides, it remains an open question whether the charge-carrier localization process can be overcome to increase catalytic yields or whether they are unavoidable, and potentially even necessary, to achieve sufficient lifetime gains. Interestingly, the trade-off between lifetime gain and energy loss observed in oxides is not unique to solids but is a central feature in the operation of the natural photosynthetic system. In photosystem II (FIG. 5d), a series of redox cofactors enable the spatial separation of the chlorophyll excited state[174]. The result is a lifetime gain of 10^6 at the expense of an energy loss of 700 meV, equivalent to 40% of the energy of a red photon[175]. Such cofactor states can be approximated as the 'molecular analogue' of intragap states in extended solids. However, the photosystem can modulate the redox cofactors to regulate the backwards and forwards electron transfer and thus displays considerable adaptability and photoconversion flexibility[176]. To achieve high photocatalytic efficiencies, the challenge is to outperform nature by decreasing or better controlling the energy losses in artificial systems. Learning to minimize unwanted defects and how to energetically and spatially control defect populations could enable the necessary fine-tuning and even reveal new materials functionality[177,178]. Achieving this goal might require the exploitation of defect–defect and polaron–defect interactions to tune energy distributions and the tolerance to unwanted defects.

Surface chemistry. The last stage in the photocatalytic process is the extraction of charges from the active material. This final step marks the start of the catalytic part of the mechanism in which photogenerated charges are extracted through a chemical reaction that occurs at the solid–liquid interface. Many reactions of interest, such as proton reduction or water oxidation, are multi-electron reactions and involve the formation and accumulation of several reactive intermediates, which means that the completion of the catalytic cycle and final product formation are slow (milliseconds to seconds)[179,180]. The role that defects have at this stage is challenging to establish. Experimentally, it is difficult to characterize the surface under operation to elucidate, at an atomic level, how the surface changes upon contact with the electrolyte or under different working conditions. This problem is not a minor issue; for example, in oxide photoanodes the mechanism of the oxygen evolution reaction (OER) has been proposed to change as a function of pivotal parameters such as the illumination intensity[181,182]. From a simulation viewpoint, it is difficult to build realistic models that describe the influence of solvation and temperature fluctuations on the frontier orbitals owing to the high computational cost. Such information is essential to explain reactivity and defect formation at the interface. Consequently, the surface of photocatalysts under working conditions is, to a great extent, uncharted territory. Nonetheless, new experimental methods and computational electrochemistry approaches are increasingly providing insight into the solid–liquid interface[82,183–190].

One of the biggest consequences of the lack of operando surface characterization is the uncertainty in the energy levels of defects, polarons and even band edges in contact with the liquid. This uncertainty means that, in many cases, it is unclear whether a given state can thermodynamically participate in redox chemistry. Thus, there have been contrasting interpretations of the role of defects, with some reports suggesting that defects have positive effects and mediate catalytic reactions,

whereas others propose that defects are unreactive, detrimental and should be eliminated or passivated[191–194]. From a reactivity standpoint, defects have several fundamental roles in the surface chemistry. First, defects can form as part of the catalytic cycle and the interaction with the electrolyte[195,196] (FIG. 6a). Second, the presence of defects can 'physically' change the nature of the surface by, for example, exposing new reactive sites[197] (FIG. 6b). Third, defects can modulate the availability of electronic charge at the surface and the charge transport between surface sites[85,92,167] (FIG. 6c). Finally, the presence of defects can modulate the energetics of the surface by, for example, altering the energy of reaction intermediates, facilitating the adsorption of molecules and even modifying the magnetic properties of the surface[198–202] (FIG. 6d).

Given the abundance of oxygen atoms in oxides, the formation of oxygen vacancies is particularly important, especially in water-based electrolytes. In perovskite electrocatalysts, ^{18}O isotope labelling mass spectrometry has shown that the O_2 evolved during the OER can come from the lattice as opposed to exclusively from water[203] (FIG. 6e). The activation of lattice oxygen and vacancy formation during the catalytic cycle (with their subsequent 're-filling') has not been extensively studied in photocatalysis, but is a possible route towards increasing the redox activity. As expected from the discussion above, whether vacancies are generated will depend on the metal–oxygen bonding and the nature of the frontier orbitals. Such effects have been systematically studied in oxide electrocatalysts, revealing that higher bond covalency increases the O 2*p* character near the Fermi level and favours the participation of lattice oxygen atoms during catalysis[203,204]. Control over the covalency and an increase in the overlap between the metal and oxygen orbitals can be achieved by lowering the energy of the cation (by using a more electronegative metal) or through incorporation of 4*d* cations with more spatially extended orbitals[195] (FIG. 1c). The crucial aspect is that in these covalent systems, the band structure allows for the creation of holes in the oxygen band, thus enabling vacancy formation. This feature might also be the case in oxide photocatalysts. For example, photoelectron spectroscopy studies on $BiVO_4$ have shown that upon exposure to water, the V and Bi atoms are reduced and the oxygen content at the surface decreases owing to the formation of oxygen vacancies[196]. Such findings emphasize the importance of oxygen vacancies at the solid–liquid interface and emphasize the need for surface characterization and labelling studies to expose the role of lattice oxygen in photocatalytic reactions[205–209].

In addition to their participation in the catalytic cycle, oxygen vacancies in $BiVO_4$ can alter the surface reactivity towards the OER. This effect has been proposed to occur by two mechanisms, namely by activating the V atoms, and thus increasing the number of active sites, and by changing the energy of adsorbates and increasing hole transfer[197]. Moreover, the presence of vacancies also increases excess charge at the surface, which has possible implications for the reactivity. In WO_3, this surface defect has been calculated to be favourably positioned to transfer electrons to OH, possibly forming OH^-. Subsequently, delocalized surface holes might transform OH^- into a reactive $OH^•$ intermediate. Crucially, in WO_3, the excess charge due to the vacancy has been proposed to form a delocalized large polaron (1 nm in diameter)[92] (FIG. 6f). Control over polaron formation at the surface is imperative, as, for example, recent measurements have shown that the rate-determining step in the OER on α-Fe_2O_3 involves a triply oxidized cluster[210]. The accumulation of three oxidation equivalents on one specific site requires the lateral diffusion of holes over the surface and, consequently, necessitates an efficient transport mechanism (note that strong polaron localization with high binding energies also leads to a higher activation barrier for charge hopping, as discussed above).

The changes that defects such as dopants or vacancies have on the surface chemistry can be more intricate than the addition of excess charge or the exposure of new sites. For example, recent experimental work has shown that tuning the concentration of Ti vacancies in

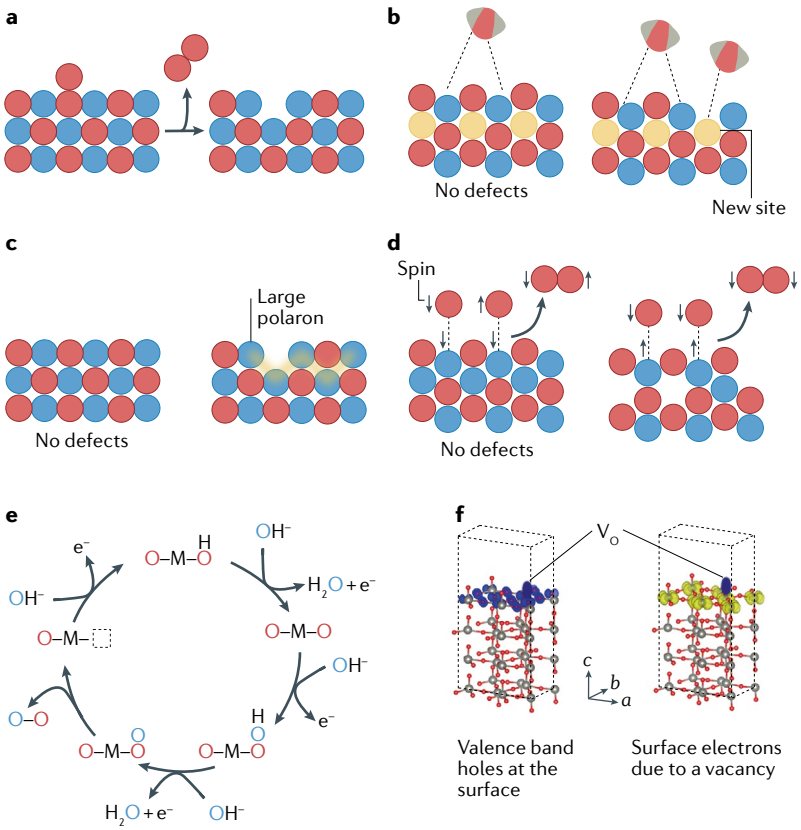

Fig. 6 | **Role of defects in surface catalysis. a** | Formation of an oxygen vacancy (V_O) during catalysis. During the oxygen evolution reaction (OER), the evolved O_2 might contain a lattice oxygen atom. **b** | The formation of defects can expose new active sites that help to enhance catalytic activity. **c** | Excess charge associated with defects can localize at the surface, forming small and large polarons. Such localization will dictate the ability of charge to diffuse to and accumulate on one site. **d** | The formation of defects can alter the surface properties by, for example, changing the surface spin polarization and favouring the parallel alignment of spins. This effect might affect spin-restricted reactions. **e** | A possible mechanism of the OER involving the formation of an oxygen vacancy (where M is a metal). The evolved O_2 contains oxygen atoms from water and the metal oxide lattice. **f** | Valence-band holes (blue) and excess electrons (yellow) associated with a vacancy at the surface of WO_3. The holes at the valence-band maximum originate from O 2*p* orbitals, whereas the electrons originate from W 5*d* orbitals. Oxygen is shown in red and tungsten in grey. Panel **e** adapted from REF.[203], Springer Nature Limited. Panel **f** adapted from REF.[92], Springer Nature Limited.

TiO_2 provides an approach to alter the spin polarization in the system and enhance photocatalytic hydrogen evolution and phenol degradation[200]. An increase in the concentration of Ti vacancies increases the population of electrons in minority spin states. This electronic polarization favours the formation of spin-polarized carriers upon photoexcitation and was suggested to influence the recombination of hydroxyl radical intermediates through spin-restriction processes (that is, a spin-selective electron exchange with OH^- species in solution). Such magnetic effects are not exclusive to TiO_2; the use of magnetic fields has been proposed to enhance the OER with Ni–Fe oxide electrocatalysts by favouring the spin-parallel alignment of oxygen radicals during O–O bond formation[211]. These advances suggest that tuning the spin polarization of the active layer, through magnetic fields or defect formation, could provide a new avenue to boost photocatalytic reactions.

Comparison with other photocatalysts

Although this Review focuses on metal oxides, an awareness of defect states is important for any photocatalyst. We therefore end with a brief comparison to defects in other photocatalytic materials to put the defect chemistry of oxides into perspective.

Organic photocatalysts

Organic polymers have become popular photocatalysts because of their high synthetic tunability and are emerging as promising photocatalyst candidates. This high synthetic tunability has sparked the creation of diverse polymeric materials with varying degrees of light absorption, conjugation, porosity and hydrophilicity, among other properties[212–214]. The most prominent examples of polymeric photocatalysts are carbon nitrides, CN_xH_y, which are based on triazine or heptazine units and possess bandgaps of 2.7 eV (REF.[215]). Like metal oxides, carbon nitrides have been explored for several catalytic reactions, such as H_2 evolution, O_2 evolution, CO_2 reduction and pollutant degradation[216].

Although the nature of the frontier orbital is clearly different to that of oxides, increasing evidence suggests that the activity of newly developed carbon nitride photocatalysts is also strongly affected by their defect chemistry in a similar way to oxides. Spectroscopic studies indicate that charge trapping in urea-derived materials results in energy losses of ~1.5 eV (about half the energy of absorbed photons), substantially decreasing the reactivity of photogenerated charges and suggesting that deeply trapped long-lived electrons are unreactive for photoreduction[217,218] (FIG. 5d). By contrast, in melamine-derived carbon nitride, long-lived trapped electrons retained sufficient chemical potential to drive proton reduction, even after 12 h in the dark[219,220].

Another similarity of organic semiconductors with metal oxides is the tendency to form polarons upon photoexcitation. Polaron formation has been observed in organic photocatalysts and especially in photovoltaics. In general, polarons are detrimental to the dissociation of charge-transfer states and consequently decrease the voltage output of devices. This behaviour parallels that proposed for metal oxide photoelectrochemical cells. What is most interesting is that, experimentally, efficient organic systems do not require band states for charge separation, indicating that the detrimental influence of polaronic effects can be lessened by materials engineering[221]. Similar synthetic strategies to those developed for organics could potentially be applied to oxide photocatalysts in order to circumvent polaron-associated losses.

Despite the big differences between carbon-based and inorganic photocatalysis, it is apparent that they share similar molecular-scale principles in relation to defect chemistry. These similarities offer an exciting opportunity to draw comparisons between these systems and, for example, to use the synthetic tunability of organics to devise defect-control strategies that are also applicable to oxides.

Metal halide perovskites

Organic–inorganic (for example, $CH_3NH_3PbI_3$) and inorganic (for example, $CsPbI_3$) halide perovskites are increasingly being explored for photocatalytic applications[222–226]. In comparison to metal oxides, these systems exhibit higher conduction-band ($E_{CBM} < E°(H_2/H^+)$) and valence-band energies ($E_{VBM} < E°(O_2/H_2O)$) and, consequently, are explored for reduction reactions or the thermodynamically facile oxidation of organic compounds[227–232].

Generally, metal halide perovskites exhibit relatively low defect formation energies and thus sustain high defect concentrations. However, they are heavily compensated systems in which the high concentrations of positively and negatively charged defects cancel, resulting in low electronic carrier concentrations. Metal halide perovskites have also proved difficult to dope, because these soft crystals can self-regulate their charge by easily forming compensating defects. Another difference to oxides is that such defects tend to be shallow in nature and, thus, relatively benign in the halides[233,234]. The shallowness of the defects is a consequence of the electronic structure, which greatly differs from that of oxides, in addition to the low carrier effective masses and the large dielectric constants (due to their polarizable structure).

The 'defect-tolerant' electronic structure of halide perovskites means that photoexcited charges retain most of their electronic energy — an advantageous feature for photocatalysis. Although there is still no consensus on the exact mechanism, increasing evidence indicates that (large) polaron formation assists in screening the excited states and helps to decrease carrier-recombination rates[235]. The formation of large polarons, as opposed to small polarons with the large binding energies typical of oxides, is due to the stronger orbital overlap that results in lower carrier effective masses[117,236–238]. Most importantly, polaronic effects can be engineered, as the softness of the material can be modulated by varying the chemical composition[239]. Metal halide perovskites are examples of materials in which the trade-off between energy loss and lifetime gain, characteristic of photocatalytic oxides and the natural photosynthetic system, can be more readily optimized.

The major limiting factor of metal halide perovskites for photocatalysis is their poor stability, especially in

polar solvents and under illumination. For example, when exposed to water the material tends to suffer surface reconstructions, forming grain boundaries. Mixed halide perovskites tend to undergo phase separation under constant illumination[240], and the facile formation of iodine vacancies can promote degradation because the excess charge associated with the vacancy reacts with O_2 to form superoxide (O_2^-). However, further studies are required to unveil the role of defects in photocatalytic perovskites, as this might differ from their role in solar cells. For example, recent work studying the degradation of an organic compound has shown that iodide vacancies are the central species that dictate photocatalytic activity[228].

Outlook

A big part of the challenge facing photocatalysis involves balancing the supply and demand of reactive charges by coordinating the charge-generation and charge-separation steps with efficient charge extraction. Kinetically, this requires the generation of charge carriers that survive long enough to supply a catalytic active site and support high turnover numbers. Energetically, such long-lived carriers must retain sufficient free energy to drive the desired chemical transformation. In a solar cell, this synchronization is relatively simple, and in photosystem II, it is achieved through a series of complex and dynamic structures within the protein frameworks. Although such structures are difficult to replicate synthetically, defect engineering might provide the chemical complexity and tunability needed to improve artificial systems.

From a materials viewpoint, optimizing the trade-off between lifetime gain and energy loss will require several advances. It will be necessary to go beyond present doping strategies and learn to control sub-bandgap states using defect–defect and defect–polaron interactions. Moreover, polaron-engineering strategies in oxides should be explored by synthetically tuning the metal coordination environment and altering the structural softness. Experimentally, such advances will require the in situ characterization of defects and polarons during operation and an investigation of how the complicated energy landscape that defects generate is affected by the catalytic conditions. Such studies should be guided by detailed theoretical work that pushes beyond the current standard of studying isolated defects in a perfect host at 0 K, instead exploring systems at room temperature and equilibrated with liquid electrolytes, to account for the multiple configurations that vacancies and other defect species can assume, both in the bulk and the at crystal boundaries.

Published online 4 May 2022

1. Gerischer, H. Electrochemical behavior of semiconductors under illumination. *J. Electrochem. Soc.* **113**, 1174 (1966).
2. Fujishima, A. & Honda, K. Electrochemical photolysis of water at a semiconductor electrode. *Nature* **238**, 37–38 (1972).
3. Pinaud, B. A. et al. Technical and economic feasibility of centralized facilities for solar hydrogen production via photocatalysis and photoelectrochemistry. *Energy Environ. Sci.* **6**, 1983–2002 (2013).
4. Wang, Q. & Domen, K. Particulate photocatalysts for light-driven water splitting: mechanisms, challenges, and design strategies. *Chem. Rev.* **120**, 919–985 (2020).
5. Abdi, F. F. et al. Efficient solar water splitting by enhanced charge separation in a bismuth vanadate-silicon tandem photoelectrode. *Nat. Commun.* **4**, 2195 (2013).
6. Pan, L. et al. Cu_2O photocathodes with band-tail states assisted hole transport for standalone solar water splitting. *Nat. Commun.* **11**, 318 (2020).
7. Kay, A., Cesar, I. & Grätzel, M. New benchmark for water photooxidation by nanostructured α-Fe_2O_3 films. *J. Am. Chem. Soc.* **128**, 15714–15721 (2006).
8. Pihosh, Y. et al. Photocatalytic generation of hydrogen by core-shell WO_3/$BiVO_4$ nanorods with ultimate water splitting efficiency. *Sci. Rep.* **5**, 11141 (2015).
9. Takata, T. et al. Photocatalytic water splitting with a quantum efficiency of almost unity. *Nature* **581**, 411–414 (2020).
10. Kim, S., Park, J. S. & Walsh, A. Identification of killer defects in kesterite thin-film solar cells. *ACS Energy Lett.* **3**, 496–500 (2018).
11. Zhang, S. X. et al. Niobium doped TiO_2: intrinsic transparent metallic anatase versus highly resistive rutile phase. *J. Appl. Phys.* **102**, 013701 (2007).
12. Corby, S., Francàs, L., Kafizas, A. & Durrant, J. R. Determining the role of oxygen vacancies in the photoelectrocatalytic performance of WO_3 for water oxidation. *Chem. Sci.* **11**, 2907–2914 (2020).
13. Moss, B. et al. Linking in situ charge accumulation to electronic structure in doped $SrTiO_3$ reveals design principles for hydrogen-evolving photocatalysts. *Nat. Mater.* **20**, 511–517 (2021).
14. Carneiro, L. M. et al. Excitation-wavelength-dependent small polaron trapping of photoexcited carriers in α-Fe_2O_3. *Nat. Mater.* **16**, 819–825 (2017).
15. Bandaranayake, S., Hruska, E., Londo, S., Biswas, S. & Baker, L. R. Small polarons and surface defects in metal oxide photocatalysts studied using XUV reflection–absorption spectroscopy. *J. Phys. Chem. C* **124**, 22853–22870 (2020).
16. Kumar, A., Kumar, A. & Krishnan, V. Perovskite oxide based materials for energy and environment-oriented photocatalysis. *ACS Catal.* **10**, 10253–10315 (2020).
17. Liu, Q. et al. Aligned Fe_2TiO_5-containing nanotube arrays with low onset potential for visible-light water oxidation. *Nat. Commun.* **5**, 5122 (2014).
18. Zhu, X. et al. Spinel structural disorder influences solar-water-splitting performance of $ZnFe_2O_4$ nanorod photoanodes. *Adv. Mater.* **30**, 1801612 (2018).
19. Xu, C., Ravi Anusuyadevi, P., Aymonier, C., Luque, R. & Marre, S. Nanostructured materials for photocatalysis. *Chem. Soc. Rev.* **48**, 3868–3902 (2019).
20. Luo, J. et al. Cu_2O nanowire photocathodes for efficient and durable solar water splitting. *Nano Lett.* **16**, 1848–1857 (2016).
21. Paracchino, A., Laporte, V., Sivula, K., Grätzel, M. & Thimsen, E. Highly active oxide photocathode for photoelectrochemical water reduction. *Nat. Mater.* **10**, 456–461 (2011).
22. Osterloh, F. E. Inorganic materials as catalysts for photochemical splitting of water. *Chem. Mater.* **20**, 35–54 (2008).
23. Henning, R. A. et al. Characterization of MFe_2O_4 (M = Mg, Zn) thin films prepared by pulsed laser deposition for photoelectrochemical applications. *J. Phys. Chem. C* **123**, 18240–18247 (2019).
24. Liu, R., Zheng, Z., Spurgeon, J. & Yang, X. Enhanced photoelectrochemical water-splitting performance of semiconductors by surface passivation layers. *Energy Environ. Sci.* **7**, 2504–2517 (2014).
25. Lee, D. K., Lee, D., Lumley, M. A. & Choi, K.-S. Progress on ternary oxide-based photoanodes for use in photoelectrochemical cells for solar water splitting. *Chem. Soc. Rev.* **48**, 2126–2157 (2019).
26. Akiyama, S. et al. Highly efficient water oxidation photoanode made of surface modified $LaTiO_2N$ particles. *Small* **12**, 5468–5476 (2016).
27. Ulmer, U. et al. Fundamentals and applications of photocatalytic CO_2 methanation. *Nat. Commun.* **10**, 3169 (2019).
28. Zhang, L. et al. Photoelectrocatalytic arene C–H amination. *Nat. Catal.* **2**, 366–373 (2019).
29. Lingampalli, S. R., Ayyub, M. M. & Rao, C. N. R. Recent progress in the photocatalytic reduction of carbon dioxide. *ACS Omega* **2**, 2740–2748 (2017).
30. Liu, L., Zhao, H., Andino, J. M. & Li, Y. Photocatalytic CO_2 reduction with H_2O on TiO_2 nanocrystals: comparison of anatase, rutile, and brookite polymorphs and exploration of surface chemistry. *ACS Catal.* **2**, 1817–1828 (2012).
31. Schreck, M. & Niederberger, M. Photocatalytic gas phase reactions. *Chem. Mater.* **31**, 597–618 (2019).
32. Jeong, S. et al. Selectivity modulated by surface ligands on Cu_2O/TiO_2 catalysts for gas-phase photocatalytic reduction of carbon dioxide. *J. Phys. Chem. C* **123**, 29184–29191 (2019).
33. Huang, C., Li, Z. & Zou, Z. A perspective on perovskite oxide semiconductor catalysts for gas phase photoreduction of carbon dioxide. *MRS Commun.* **6**, 216–225 (2016).
34. Sivula, K., Le Formal, F. & Grätzel, M. Solar water splitting: progress using hematite (α-Fe_2O_3) photoelectrodes. *ChemSusChem* **4**, 432–449 (2011).
35. Cesar, I., Kay, A., Gonzalez Martinez, J. A. & Grätzel, M. Translucent thin film Fe_2O_3 photoanodes for efficient water splitting by sunlight: nanostructure-directing effect of Si-doping. *J. Am. Chem. Soc.* **128**, 4582–4583 (2006).
36. Kim, J. Y. et al. Single-crystalline, wormlike hematite photoanodes for efficient solar water splitting. *Sci. Rep.* **3**, 2681 (2013).
37. Grave, D. A., Yatom, N., Ellis, D. S., Toroker, M. C. & Rothschild, A. The "rust" challenge: on the correlations between electronic structure, excited state dynamics, and photoelectrochemical performance of hematite photoanodes for solar water splitting. *Adv. Mater.* **30**, 1706577 (2018).
38. Gardecka, A. J. et al. High efficiency water splitting photoanodes composed of nano-structured anatase-rutile TiO_2 heterojunctions by pulsed-pressure MOCVD. *Appl. Catal. B* **224**, 904–911 (2018).
39. Roy, P. et al. Oxide nanotubes on Ti–Ru alloys: strongly enhanced and stable photoelectrochemical activity for water splitting. *J. Am. Chem. Soc.* **133**, 5629–5631 (2011).
40. Liu, M., de Leon Snapp, N. & Park, H. Water photolysis with a cross-linked titanium dioxidenanowire anode. *Chem. Sci.* **2**, 80–87 (2011).
41. Fàbrega, C. et al. Efficient WO_3 photoanodes fabricated by pulsed laser deposition for photoelectrochemical water splitting with high Faradaic efficiency. *Appl. Catal. B* **189**, 133–140 (2016).
42. Wang, S. et al. Synergistic crystal facet engineering and structural control of WO_3 films exhibiting unprecedented photoelectrochemical performance. *Nano Energy* **24**, 94–102 (2016).

43. Brillet, J. et al. Highly efficient water splitting by a dual-absorber tandem cell. *Nat. Photon.* **6**, 824–828 (2012).
44. Kim, T. W. & Choi, K.-S. Nanoporous $BiVO_4$ photoanodes with dual-layer oxygen evolution catalysts for solar water splitting. *Science* **343**, 990–994 (2014).
45. Qiu, Y. et al. Efficient solar-driven water splitting by nanocone $BiVO_4$-perovskite tandem cells. *Sci. Adv.* **2**, e1501764 (2016).
46. Wang, S. et al. New $BiVO_4$ dual photoanodes with enriched oxygen vacancies for efficient solar-driven water splitting. *Adv. Mater.* **30**, 1800486 (2018).
47. Hayes W & Stoneham, A. M. *Defects and Defect Processes in Nonmetallic Solids* (Dover, 2004).
48. Li, W., Shi, J., Zhang, K. H. L. & MacManus-Driscoll, J. L. Defects in complex oxide thin films for electronics and energy applications: challenges and opportunities. *Mater. Horiz.* **7**, 2832–2859 (2020).
49. Biswas, S., Husek, J., Londo, S. & Baker, L. R. Ultrafast electron trapping and defect-mediated recombination in NiO probed by femtosecond extreme ultraviolet reflection–absorption spectroscopy. *J. Phys. Chem. Lett.* **9**, 5047–5054 (2018).
50. Wei, Y., Zhou, Z., Fang, W.-H. & Long, R. Grain boundary facilitates photocatalytic reaction in rutile TiO_2 despite fast charge recombination: a time-domain ab initio analysis. *J. Phys. Chem. Lett.* **9**, 5884–5889 (2018).
51. Bai, S., Zhang, N., Gao, C. & Xiong, Y. Defect engineering in photocatalytic materials. *Nano Energy* **53**, 296–336 (2018).
52. Kröger, F. A. *The Chemistry of Imperfect Crystals: Preparation, Purification, Crystal Growth and Phase Theory* Vol. 1–3 (North-Holland, 1973).
53. de Groot, F. M. F. et al. Oxygen 1*s* X-ray-absorption edges of transition-metal oxides. *Phys. Rev. B* **40**, 5715–5723 (1989).
54. Arima, T., Tokura, Y. & Torrance, J. B. Variation of optical gaps in perovskite-type 3*d* transition-metal oxides. *Phys. Rev. B* **48**, 17006–17009 (1993).
55. Lany, S. Semiconducting transition metal oxides. *J. Phys. Condens. Matter* **27**, 283203 (2015).
56. Hwang, J. et al. Perovskites in catalysis and electrocatalysis. *Science* **358**, 751–756 (2017).
57. Grimaud, A. et al. Double perovskites as a family of highly active catalysts for oxygen evolution in alkaline solution. *Nat. Commun.* **4**, 2439 (2013).
58. Hong, W. T. et al. Toward the rational design of non-precious transition metal oxides for oxygen electrocatalysis. *Energy Environ. Sci.* **8**, 1404–1427 (2015).
59. Calle-Vallejo, F. et al. Number of outer electrons as descriptor for adsorption processes on transition metals and their oxides. *Chem. Sci.* **4**, 1245 (2013).
60. Nie, X., Wei, S.-H. & Zhang, S. B. First-principles study of transparent p-type conductive $SrCu_2O_2$ and related compounds. *Phys. Rev. B* **65**, 075111 (2002).
61. Greiner, M. T. & Lu, Z.-H. Thin-film metal oxides in organic semiconductor devices: their electronic structures, work functions and interfaces. *npg Asia Mater.* **5**, e55 (2013).
62. Zawadzki, P., Jacobsen, K. W. & Rossmeisl, J. Electronic hole localization in rutile and anatase TiO_2 — self-interaction correction in Δ-SCF DFT. *Chem. Phys. Lett.* **506**, 42–45 (2011).
63. Tuller, H. L. & Bishop, S. R. Point defects in oxides: tailoring materials through defect engineering. *Annu. Rev. Mater. Res.* **41**, 369–398 (2011).
64. Park, J. S., Kim, S., Xie, Z. & Walsh, A. Point defect engineering in thin-film solar cells. *Nat. Rev. Mater.* **3**, 194–210 (2018).
65. Sai Gautam, G., Senftle, T. P., Alidoust, N. & Carter, E. A. Novel solar cell materials: insights from first-principles. *J. Phys. Chem. C* **122**, 27107–27126 (2018).
66. Zhang, S. & Northrup, J. Chemical potential dependence of defect formation energies in GaAs: application to Ga self-diffusion. *Phys. Rev. Lett.* **67**, 2339–2342 (1991).
67. Buckeridge, J. Equilibrium point defect and charge carrier concentrations in a material determined through calculation of the self-consistent Fermi energy. *Comput. Phys. Commun.* **244**, 329–342 (2019).
68. Fernández-Climent, R., Giménez, S. & García-Tecedor, M. The role of oxygen vacancies in water splitting photoanodes. *Sustain. Energy Fuels* **4**, 5916–5926 (2020).
69. Wexler, R. B., Gautam, G. S., Stechel, E. B. & Carter, E. A. Factors governing oxygen vacancy formation in oxide perovskites. *J. Am. Chem. Soc.* **143**, 13212–13227 (2021).
70. Muñoz-García, A. B., Ritzmann, A. M., Pavone, M., Keith, J. A. & Carter, E. A. Oxygen transport in perovskite-type solid oxide fuel cell materials: insights from quantum mechanics. *Acc. Chem. Res.* **47**, 3340–3348 (2014).
71. Yu, P. Y. & Cardona, M. *Fundamentals of Semiconductors* (Springer, 2010).
72. Lang, D. V. Deep-level transient spectroscopy: a new method to characterize traps in semiconductors. *J. Appl. Phys.* **45**, 3023–3032 (1974).
73. Walsh, A. & Zunger, A. Instilling defect tolerance in new compounds. *Nat. Mater.* **16**, 964–967 (2017).
74. Sachs, M. et al. Effect of oxygen deficiency on the excited state kinetics of WO_3 and implications for photocatalysis. *Chem. Sci.* **10**, 5667–5677 (2019).
75. Wang, W., Janotti, A. & Van de Walle, C. G. Role of oxygen vacancies in crystalline WO_3. *J. Mater. Chem. C* **4**, 6641–6648 (2016).
76. Zandi, O., Klahr, B. M. & Hamann, T. W. Highly photoactive Ti-doped α-Fe_2O_3 thin film electrodes: resurrection of the dead layer. *Energy Environ. Sci.* **6**, 634–642 (2013).
77. Zhong, D. K., Choi, S. & Gamelin, D. R. Near-complete suppression of surface recombination in solar photoelectrolysis by "Co-Pi" catalyst-modified W:$BiVO_4$. *J. Am. Chem. Soc.* **133**, 18370–18377 (2011).
78. Fröhlich, H. Electrons in lattice fields. *Adv. Phys.* **3**, 325–361 (1954).
79. Shluger, A. L. & Stoneham, A. M. Small polarons in real crystals: concepts and problems. *J. Phys. Condens. Matter* **5**, 3049–3086 (1993).
80. Emin, D. Optical properties of large and small polarons and bipolarons. *Phys. Rev. B* **48**, 13691–13702 (1993).
81. Rettie, A. J. E., Chemelewski, W. D., Emin, D. & Mullins, C. B. Unravelling small-polaron transport in metal oxide photoelectrodes. *J. Phys. Chem. Lett.* **7**, 471–479 (2016).
82. Rousseau, R., Glezakou, V.-A. & Selloni, A. Theoretical insights into the surface physics and chemistry of redox-active oxides. *Nat. Rev. Mater.* **5**, 460–475 (2020).
83. Franchini, C., Reticcioli, M., Setvin, M. & Diebold, U. Polarons in materials. *Nat. Rev. Mater.* **6**, 560–586 (2021).
84. Wiktor, J., Ambrosio, F. & Pasquarello, A. Role of polarons in water splitting: the case of $BiVO_4$. *ACS Energy Lett.* **3**, 1693–1697 (2018).
85. Wang, W. et al. The role of surface oxygen vacancies in $BiVO_4$. *Chem. Mater.* **32**, 2899–2909 (2020).
86. Davies, D. W. et al. Descriptors for electron and hole charge carriers in metal oxides. *J. Phys. Chem. Lett.* **11**, 438–444 (2020).
87. Meggiolaro, D., Ambrosio, F., Mosconi, E., Mahata, A. & De Angelis, F. Polarons in metal halide perovskites. *Adv. Energy Mater.* **10**, 1902748 (2019).
88. Yang, S., Brant, A. T., Giles, N. C. & Halliburton, L. E. Intrinsic small polarons in rutile TiO_2. *Phys. Rev. B* **87**, 125201 (2013).
89. Moser, S. et al. Tunable polaronic conduction in anatase TiO_2. *Phys. Rev. Lett.* **110**, 196403 (2013).
90. Moser, S. et al. Electron-phonon coupling in the bulk of anatase TiO_2 measured by resonant inelastic X-ray spectroscopy. *Phys. Rev. Lett.* **115**, 096404 (2015).
91. Setvin, M. et al. Direct view at excess electrons in TiO_2 rutile and anatase. *Phys. Rev. Lett.* **113**, 086402 (2014).
92. Gerosa, M., Gygi, F., Govoni, M. & Galli, G. The role of defects and excess surface charges at finite temperature for optimizing oxide photoabsorbers. *Nat. Mater.* **17**, 1122–1127 (2018).
93. Kweon, K. E., Hwang, G. S., Kim, J., Kim, S. & Kim, S. Electron small polarons and their transport in bismuth vanadate: a first principles study. *Phys. Chem. Chem. Phys.* **17**, 256–260 (2015).
94. Butler, K. T. et al. Ultrafast carrier dynamics in $BiVO_4$ thin film photoanode material: interplay between free carriers, trapped carriers and low-frequency lattice vibrations. *J. Mater. Chem. A* **4**, 18516–18523 (2016).
95. Qiu, W. et al. Freeing the polarons to facilitate charge transport in $BiVO_4$ from oxygen vacancies with an oxidative 2D precursor. *Angew. Chem. Int. Ed.* **58**, 19087–19095 (2019).
96. Ziwritsch, M. et al. Direct time-resolved observation of carrier trapping and polaron conductivity in $BiVO_4$. *ACS Energy Lett.* **1**, 888–894 (2016).
97. Mohamed, M. et al. The electronic structure and the formation of polarons in Mo-doped $BiVO_4$ measured by angle-resolved photoemission spectroscopy. *RSC Adv.* **9**, 15606–15614 (2019).
98. Pastor, E. et al. In situ observation of picosecond polaron self-localisation in α-Fe_2O_3 photoelectrochemical cells. *Nat. Commun.* **10**, 3962 (2019).
99. Husek, J., Cirri, A., Biswas, S. & Baker, L. R. Surface electron dynamics in hematite (α-Fe_2O_3): correlation between ultrafast surface electron trapping and small polaron formation. *Chem. Sci.* **8**, 8170–8178 (2017).
100. Zhou, Z., Long, R. & Prezhdo, O. V. Why silicon doping accelerates electron polaron diffusion in hematite. *J. Am. Chem. Soc.* **141**, 20222–20233 (2019).
101. Shelton, J. L. & Knowles, K. E. Thermally activated optical absorption into polaronic states in hematite. *J. Phys. Chem. Lett.* **12**, 3343–3351 (2021).
102. Smart, T. J., Pham, T. A., Ping, Y. & Ogitsu, T. Optical absorption induced by small polaron formation in transition metal oxides: the case of Co_3O_4. *Phys. Rev. Mater.* **3**, 102401 (2019).
103. Chen, C., Avila, J., Frantzeskakis, E., Levy, A. & Asensio, M. C. Observation of a two-dimensional liquid of Fröhlich polarons at the bare $SrTiO_3$ surface. *Nat. Commun.* **6**, 8585 (2015).
104. Biswas, S., Husek, J., Londo, S. & Baker, L. R. Highly localized charge transfer excitons in metal oxide semiconductors. *Nano Lett.* **18**, 1228–1233 (2018).
105. Pelli Cresi, J. S. et al. Ultrafast formation of small polarons and the optical gap in CeO_2. *J. Phys. Chem. Lett.* **11**, 5686–5691 (2020).
106. Biswas, S., Wallentine, S., Bandaranayake, S. & Baker, L. R. Controlling polaron formation at hematite surfaces by molecular functionalization probed by XUV reflection-absorption spectroscopy. *J. Chem. Phys.* **151**, 104701 (2019).
107. Katz, J. E. et al. Electron small polarons and their mobility in iron (oxyhydr)oxide nanoparticles. *Science* **337**, 1200–1203 (2012).
108. Porter, I. J. et al. Photoexcited small polaron formation in goethite (α-FeOOH) nanorods probed by transient extreme ultraviolet spectroscopy. *J. Phys. Chem. Lett.* **9**, 4120–4124 (2018).
109. Vura-Weis, J. et al. Femtosecond $M_{2,3}$-edge spectroscopy of transition-metal oxides: photoinduced oxidation state change in α-Fe_2O_3. *J. Phys. Chem. Lett.* **4**, 3667–3671 (2013).
110. Chen, W. & Xiong, W. Polaron-formation revealed by transient XUV imaginary refractive index changes in different iron compounds. *Phys. Chem. Chem. Phys.* **23**, 4486–4490 (2021).
111. Biswas, S., Husek, J. & Baker, L. R. Elucidating ultrafast electron dynamics at surfaces using extreme ultraviolet (XUV) reflection–absorption spectroscopy. *Chem. Commun.* **54**, 4216–4230 (2018).
112. Santomauro, F. G. et al. Femtosecond X-ray absorption study of electron localization in photoexcited anatase TiO_2. *Sci. Rep.* **5**, 14834 (2015).
113. Obara, Y. et al. Femtosecond time-resolved X-ray absorption spectroscopy of anatase TiO_2 nanoparticles using XFEL. *Struct. Dyn.* **4**, 044033 (2017).
114. Ismail, A. S. M. et al. Direct observation of the electronic states of photoexcited hematite with ultrafast 2*p*3*d* X-ray absorption spectroscopy and resonant inelastic X-ray scattering. *Phys. Chem. Chem. Phys.* **22**, 2685–2692 (2020).
115. Abdi, F. F., Savenije, T. J., May, M. M., Dam, B. & Van De Krol, R. The origin of slow carrier transport in $BiVO_4$ thin film photoanodes: a time-resolved microwave conductivity study. *J. Phys. Chem. Lett.* **4**, 2752–2757 (2013).
116. Frost, J. M. & Walsh, A. What is moving in hybrid halide perovskite solar cells? *Acc. Chem. Res.* **49**, 528–535 (2016).
117. Ghosh, D., Welch, E., Neukirch, A. J., Zakhidov, A. & Tretiak, S. Polarons in halide perovskites: a perspective. *J. Phys. Chem. Lett.* **11**, 3271–3286 (2020).
118. Li, J. & Wu, N. Semiconductor-based photocatalysts and photoelectrochemical cells for solar fuel generation: a review. *Catal. Sci. Technol.* **5**, 1360–1384 (2015).
119. Durrant, J. R. Molecular approaches to solar energy conversion: the energetic cost of charge separation from molecular-excited states. *Phil. Trans. R. Soc. A* **371**, 20120195 (2013).
120. Barroso, M., Pendlebury, S. R., Cowan, A. J. & Durrant, J. R. Charge carrier trapping, recombination and transfer in hematite (α-Fe_2O_3) water splitting photoanodes. *Chem. Sci.* **4**, 2724 (2013).
121. Tan, M. X. et al. in *Progress in Inorganic Chemistry* (ed. Karlin, K. D.) 21–144 (Wiley, 1994).
122. Yang, Y. et al. Progress in developing metal oxide nanomaterials for photoelectrochemical water splitting. *Adv. Energy Mater.* **7**, 1700555 (2017).

123. Borgarello, E., Kiwi, J., Graetzel, M., Pelizzetti, E. & Visca, M. Visible light induced water cleavage in colloidal solutions of chromium-doped titanium dioxide particles. *J. Am. Chem. Soc.* **104**, 2996–3002 (1982).
124. Choi, W., Termin, A. & Hoffmann, M. R. The role of metal ion dopants in quantum-sized TiO_2: correlation between photoreactivity and charge carrier recombination dynamics. *J. Phys. Chem.* **98**, 13669–13679 (1994).
125. Konta, R., Ishii, T., Kato, H. & Kudo, A. Photocatalytic activities of noble metal ion doped $SrTiO_3$ under visible light irradiation. *J. Phys. Chem. B* **108**, 8992–8995 (2004).
126. Asahi, R., Morikawa, T., Irie, H. & Ohwaki, T. Nitrogen-doped titanium dioxide as visible-light-sensitive photocatalyst: designs, developments, and prospects. *Chem. Rev.* **114**, 9824–9852 (2014).
127. Ansari, S. A., Khan, M. M., Ansari, M. O. & Cho, M. H. Nitrogen-doped titanium dioxide (N-doped TiO_2) for visible light photocatalysis. *N. J. Chem.* **40**, 3000–3009 (2016).
128. Suzuki, H., Tomita, O., Higashi, M. & Abe, R. Design of nitrogen-doped layered tantalates for non-sacrificial and selective hydrogen evolution from water under visible light. *J. Mater. Chem. A* **4**, 14444–14452 (2016).
129. Xia, T. et al. Hydrogenated black ZnO nanoparticles with enhanced photocatalytic performance. *RSC Adv.* **4**, 41654–41658 (2014).
130. Guo, H.-L. et al. Oxygen deficient ZnO_{1-x} nanosheets with high visible light photocatalytic activity. *Nanoscale* **7**, 7216–7223 (2015).
131. Fan, C.-M. et al. Synproportionation reaction for the fabrication of Sn^{2+} self-doped SnO_{2-x} nanocrystals with tunable band structure and highly efficient visible light photocatalytic activity. *J. Phys. Chem. C* **117**, 24157–24166 (2013).
132. Chen, X., Liu, L. & Huang, F. Black titanium dioxide (TiO_2) nanomaterials. *Chem. Soc. Rev.* **44**, 1861–1885 (2015).
133. Chen, X., Liu, L., Yu, P. Y. & Mao, S. S. Increasing solar absorption for photocatalysis with black hydrogenated titanium dioxide nanocrystals. *Science* **331**, 746–750 (2011).
134. Xu, X. et al. Black $BiVO_4$: size tailored synthesis, rich oxygen vacancies, and sodium storage performance. *J. Mater. Chem. A* **8**, 1636–1645 (2020).
135. Kawasaki, S. et al. Elucidation of Rh-induced in-gap states of Rh:$SrTiO_3$ visible-light-driven photocatalyst by soft X-ray spectroscopy and first-principles calculations. *J. Phys. Chem. C* **116**, 24445–24448 (2012).
136. Murthy, D. H. K. et al. Revealing the role of the Rh valence state, La doping level and Ru cocatalyst in determining the H_2 evolution efficiency in doped $SrTiO_3$ photocatalysts. *Sustain. Energy Fuels* **3**, 208–218 (2019).
137. Wang, G. et al. Hydrogen-treated WO_3 nanoflakes show enhanced photostability. *Energy Environ. Sci.* **5**, 6180 (2012).
138. Ling, M. et al. Correlation of optical properties, electronic structure, and photocatalytic activity in nanostructured tungsten oxide. *Adv. Mater. Interfaces* **4**, 1700064 (2017).
139. Deb, S. K. Opportunities and challenges in science and technology of WO_3 for electrochromic and related applications. *Sol. Energy Mater. Sol. Cell* **92**, 245–258 (2008).
140. Powell, A. W., Stavrinadis, A., Christodoulou, S., Quidant, R. & Konstantatos, G. On-demand activation of photochromic nanoheaters for high color purity 3D printing. *Nano Lett.* **20**, 3485–3491 (2020).
141. Chatten, R., Chadwick, A. V., Rougier, A. & Lindan, P. J. D. The oxygen vacancy in crystal phases of WO_3. *J. Phys. Chem. B* **109**, 3146–3156 (2005).
142. Bange, K. Coloration of tungsten oxide films: a model for optically active coatings. *Sol. Energy Mater. Sol. Cell* **58**, 1–131 (1999).
143. Dixon, R. A. et al. Electronic states at oxygen deficient WO_3(001) surfaces: a study by resonant photoemission. *Surf. Sci.* **399**, 199–211 (1998).
144. Zhang, S. B., Wei, S.-H., Zunger, A. & Katayama-Yoshida, H. Defect physics of the $CuInSe_2$ chalcopyrite semiconductor. *Phys. Rev. B* **57**, 9642–9656 (1998).
145. Grave, D. A. et al. Extraction of mobile charge carrier photogeneration yield spectrum of ultrathin-film metal oxide photoanodes for solar water splitting. *Nat. Mater.* **20**, 833–840 (2021).
146. Kennedy, J. H. & Frese, K. W. Photooxidation of water at α-Fe_2O_3 electrodes. *J. Electrochem. Soc.* **125**, 709–714 (1978).
147. Huang, Z. et al. In situ probe of photocarrier dynamics in water-splitting hematite (α-Fe_2O_3) electrodes. *Energy Environ. Sci.* **5**, 8923 (2012).
148. Hayes, D. et al. Electronic and nuclear contributions to time-resolved optical and X-ray absorption spectra of hematite and insights into photoelectrochemical performance. *Energy Environ. Sci.* **9**, 3754–3769 (2016).
149. Miao, C., Shi, T., Xu, G., Ji, S. & Ye, C. Photocurrent enhancement for Ti-doped Fe_2O_3 thin film photoanodes by an in situ solid-state reaction method. *ACS Appl. Mater. Interfaces* **5**, 1310–1316 (2013).
150. Zhao, B. et al. Electrical transport properties of Ti-doped Fe_2O_3 (0001) epitaxial films. *Phys. Rev. B* **84**, 245325 (2011).
151. Wang, G. et al. Facile synthesis of highly photoactive α-Fe_2O_3-based films for water oxidation. *Nano Lett.* **11**, 3503–3509 (2011).
152. Smart, T. J. & Ping, Y. Effect of defects on the small polaron formation and transport properties of hematite from first-principles calculations. *J. Phys. Condens. Matter* **29**, 394006 (2017).
153. Ling, Y., Wang, G., Wheeler, D. A., Zhang, J. Z. & Li, Y. Sn-doped hematite nanostructures for photoelectrochemical water splitting. *Nano Lett.* **11**, 2119–2125 (2011).
154. Liu, J. et al. Highly oriented Ge-doped hematite nanosheet arrays for photoelectrochemical water oxidation. *Nano Energy* **9**, 282–290 (2014).
155. Berglund, S. P., Rettie, A. J. E., Hoang, S. & Mullins, C. B. Incorporation of Mo and W into nanostructured $BiVO_4$ films for efficient photoelectrochemical water oxidation. *Phys. Chem. Chem. Phys.* **14**, 7065–7075 (2012).
156. Luo, W. et al. Solar hydrogen generation from seawater with a modified $BiVO_4$ photoanode. *Energy Environ. Sci.* **4**, 4046 (2011).
157. Zhao, X., Hu, J., Chen, S. & Chen, Z. An investigation on the role of W doping in $BiVO_4$ photoanodes used for solar water splitting. *Phys. Chem. Chem. Phys.* **20**, 13637–13645 (2018).
158. Ludwig, G. W. & Watters, R. L. Drift and conductivity mobility in silicon. *Phys. Rev.* **101**, 1699–1701 (1956).
159. Cronemeyer, D. C. Hall and drift mobility in high-resistivity single-crystal silicon. *Phys. Rev.* **105**, 522–523 (1957).
160. Rosso, K. M., Smith, D. M. A. & Dupuis, M. An ab initio model of electron transport in hematite (α-Fe_2O_3) basal planes. *J. Chem. Phys.* **118**, 6455–6466 (2003).
161. Iordanova, N., Dupuis, M. & Rosso, K. M. Charge transport in metal oxides: a theoretical study of hematite α-Fe_2O_3. *J. Chem. Phys.* **122**, 144305 (2005).
162. Zhang, L. et al. Significantly enhanced photocurrent for water oxidation in monolithic Mo:$BiVO_4$/SnO_2/Si by thermally increasing the minority carrier diffusion length. *Energy Environ. Sci.* **9**, 2044–2052 (2016).
163. Selim, S. et al. Impact of oxygen vacancy occupancy on charge carrier dynamics in $BiVO_4$ photoanodes. *J. Am. Chem. Soc.* **141**, 18791–18798 (2019).
164. Cooper, J. K. et al. Role of hydrogen in defining the n-type character of $BiVO_4$ photoanodes. *Chem. Mater.* **28**, 5761–5771 (2016).
165. Seo, H., Ping, Y. & Galli, G. Role of point defects in enhancing the conductivity of $BiVO_4$. *Chem. Mater.* **30**, 7793–7802 (2018).
166. Rossell, M. D. et al. Direct evidence of surface reduction in monoclinic $BiVO_4$. *Chem. Mater.* **27**, 3593–3600 (2015).
167. Hegner, F. S., Forrer, D., Galán-Mascarós, J. R., López, N. & Selloni, A. Versatile nature of oxygen vacancies in bismuth vanadate bulk and (001) surface. *J. Phys. Chem. Lett.* **10**, 6672–6678 (2019).
168. Vequizo, J. J. M. et al. Trapping-induced enhancement of photocatalytic activity on brookite TiO_2 powders: comparison with anatase and rutile TiO_2 powders. *ACS Catal.* **7**, 2644–2651 (2017).
169. Moss, B. et al. Comparing photoelectrochemical water oxidation, recombination kinetics and charge trapping in the three polymorphs of TiO_2. *Sci. Rep.* **7**, 2938 (2017).
170. Corby, S. et al. The kinetics of metal oxide photoanodes from charge generation to catalysis. *Nat. Rev. Mater.* **6**, 1136–1155 (2021).
171. Corby, S. et al. Charge separation, band-bending, and recombination in WO_3 photoanodes. *J. Phys. Chem. Lett.* **10**, 5395–5401 (2019).
172. Lohaus, C., Klein, A. & Jaegermann, W. Limitation of Fermi level shifts by polaron defect states in hematite photoelectrodes. *Nat. Commun.* **9**, 4309 (2018).
173. Guijarro, N. et al. Evaluating spinel ferrites MFe_2O_4 (M = Cu, Mg, Zn) as photoanodes for solar water oxidation: prospects and limitations. *Sustain. Energy Fuels* **2**, 103–117 (2018).
174. Kato, M., Zhang, J. Z., Paul, N. & Reisner, E. Protein film photoelectrochemistry of the water oxidation enzyme photosystem II. *Chem. Soc. Rev.* **43**, 6485–6497 (2014).
175. Cowan, A. J. & Durrant, J. R. Long-lived charge separated states in nanostructured semiconductor photoelectrodes for the production of solar fuels. *Chem. Soc. Rev.* **42**, 2281–2293 (2013).
176. Kato, Y., Nagao, R. & Noguchi, T. Redox potential of the terminal quinone electron acceptor Q_B in photosystem II reveals the mechanism of electron transfer regulation. *Proc. Natl Acad. Sci. USA* **113**, 620–625 (2016).
177. Kalinin, S. V. & Spaldin, N. A. Functional ion defects in transition metal oxides. *Science* **341**, 858–859 (2013).
178. Wu, F. & Ping, Y. Combining Landau–Zener theory and kinetic Monte Carlo sampling for small polaron mobility of doped $BiVO_4$ from first-principles. *J. Mater. Chem. A* **6**, 20025–20036 (2018).
179. Pastor, E. et al. Spectroelectrochemical analysis of the mechanism of (photo)electrochemical hydrogen evolution at a catalytic interface. *Nat. Commun.* **8**, 14280 (2017).
180. Pendlebury, S. R. et al. Correlating long-lived photogenerated hole populations with photocurrent densities in hematite water oxidation photoanodes. *Energy Environ. Sci.* **5**, 6304–6312 (2012).
181. Le Formal, F. et al. Rate law analysis of water oxidation on a hematite surface. *J. Am. Chem. Soc.* **137**, 6629–6637 (2015).
182. Li, J. et al. Reaction kinetics and interplay of two different surface states on hematite photoanodes for water oxidation. *Nat. Commun.* **12**, 255 (2021).
183. Meirer, F. & Weckhuysen, B. M. Spatial and temporal exploration of heterogeneous catalysts with synchrotron radiation. *Nat. Rev. Mater.* **3**, 324–340 (2018).
184. Eichhorn, J., Jiang, C.-M., Cooper, J. K., Sharp, I. D. & Toma, F. M. Nanoscale heterogeneities and composition–reactivity relationships in copper vanadate photoanodes. *ACS Appl. Mater. Interfaces* **13**, 23575–23583 (2021).
185. Ambrosio, F., Wiktor, J. & Pasquarello, A. pH-Dependent catalytic reaction pathway for water splitting at the $BiVO_4$–water interface from the band alignment. *ACS Energy Lett.* **3**, 829–834 (2018).
186. Govind Rajan, A., Martirez, J. M. P. & Carter, E. A. Why do we use the materials and operating conditions we use for heterogeneous (photo)electrochemical water splitting? *ACS Catal.* **10**, 11177–11234 (2020).
187. Iqbal, A. & Bevan, K. H. Simultaneously solving the photovoltage and photocurrent at semiconductor–liquid interfaces. *J. Phys. Chem. C* **122**, 30–43 (2018).
188. Bhati, M., Chen, Y. & Senftle, T. P. Density functional theory modeling of photo-electrochemical reactions on semiconductors: H_2 evolution on 3C-SiC. *J. Phys. Chem. C* **124**, 26625–26639 (2020).
189. Butler, K. T., Sai Gautam, G. & Canepa, P. Designing interfaces in energy materials applications with first-principles calculations. *NPJ Comput. Mater.* **5**, 19 (2019).
190. Liao, P. & Carter, E. A. New concepts and modeling strategies to design and evaluate photo-electro-catalysts based on transition metal oxides. *Chem. Soc. Rev.* **42**, 2401–2422 (2013).
191. Shi, Q. et al. Role of tungsten doping on the surface states in $BiVO_4$ photoanodes for water oxidation: tuning the electron trapping process. *ACS Catal.* **8**, 3331–3342 (2018).
192. Zandi, O. & Hamann, T. W. Enhanced water splitting efficiency through selective surface state removal. *J. Phys. Chem. Lett.* **5**, 1522–1526 (2014).
193. Zhang, P., Wang, T. & Gong, J. Passivation of surface states by ALD-grown TiO_2 overlayers on Ta_3N_5 anodes for photoelectrochemical water oxidation. *Chem. Commun.* **52**, 8806–8809 (2016).
194. Le Formal, F. et al. Passivating surface states on water splitting hematite photoanodes with alumina overlayers. *Chem. Sci.* **2**, 737–743 (2011).
195. Grimaud, A., Hong, W. T., Shao-Horn, Y. & Tarascon, J.-M. Anionic redox processes for electrochemical devices. *Nat. Mater.* **15**, 121–126 (2016).
196. Hermans, Y., Murcia-López, S., Klein, A. & Jaegermann, W. $BiVO_4$ surface reduction upon water exposure. *ACS Energy Lett.* **4**, 2522–2528 (2019).

197. Hu, J., Zhao, X., Chen, W., Su, H. & Chen, Z. Theoretical insight into the mechanism of photoelectrochemical oxygen evolution reaction on $BiVO_4$ anode with oxygen vacancy. *J. Phys. Chem. C* **121**, 18702–18709 (2017).
198. Zhang, X., Klaver, P., van Santen, R., van de Sanden, M. C. M. & Bieberle-Hütter, A. Oxygen evolution at hematite surfaces: the impact of structure and oxygen vacancies on lowering the overpotential. *J. Phys. Chem. C* **120**, 18201–18208 (2016).
199. Liao, P., Keith, J. A. & Carter, E. A. Water oxidation on pure and doped hematite (0001) surfaces: prediction of Co and Ni as effective dopants for electrocatalysis. *J. Am. Chem. Soc.* **134**, 13296–13309 (2012).
200. Pan, L. et al. Manipulating spin polarization of titanium dioxide for efficient photocatalysis. *Nat. Commun.* **11**, 418 (2020).
201. Zhang, Y. et al. Direct observation of oxygen vacancy self-healing on TiO_2 photocatalysts for solar water splitting. *Angew. Chem. Int. Ed.* **58**, 14229–14233 (2019).
202. Huang, Y., Yu, Y., Yu, Y. & Zhang, B. Oxygen vacancy engineering in photocatalysis. *Sol. RRL* **4**, 2000037 (2020).
203. Grimaud, A. et al. Activating lattice oxygen redox reactions in metal oxides to catalyse oxygen evolution. *Nat. Chem.* **9**, 457–465 (2017).
204. Hong, W. T. et al. Charge-transfer-energy-dependent oxygen evolution reaction mechanisms for perovskite oxides. *Energy Environ. Sci.* **10**, 2190–2200 (2017).
205. Günnemann, C., Bahnemann, D. W. & Robertson, P. K. J. Isotope effects in photocatalysis: an underexplored issue. *ACS Omega* **6**, 11113–11121 (2021).
206. Civiš, S., Ferus, M., Kubát, P., Zukalová, M. & Kavan, L. Oxygen-isotope exchange between CO_2 and solid $Ti_{18}O_2$. *J. Phys. Chem. C* **115**, 11156–11162 (2011).
207. Montoya, J. F. et al. Catalytic role of surface oxygens in TiO_2 photooxidation reactions: aqueous benzene photooxidation with $Ti_{18}O_2$ under anaerobic conditions. *J. Phys. Chem. Lett.* **4**, 1415–1422 (2013).
208. Mikhaylov, R. V., Lisachenko, A. A. & Titov, V. V. Investigation of photostimulated oxygen isotope exchange on TiO_2 Degussa P25 surface upon UV–vis irradiation. *J. Phys. Chem. C* **116**, 23332–23341 (2012).
209. Courbon, H., Formenti, M. & Pichat, P. Study of oxygen isotopic exchange over ultraviolet irradiated anatase samples and comparison with the photooxidation of isobutane into acetone. *J. Phys. Chem.* **81**, 550–554 (1977).
210. Mesa, C. A. et al. Multihole water oxidation catalysis on haematite photoanodes revealed by operando spectroelectrochemistry and DFT. *Nat. Chem.* **12**, 82–89 (2020).
211. Garcés-Pineda, F. A., Blasco-Ahicart, M., Nieto-Castro, D., López, N. & Galán-Mascarós, J. R. Direct magnetic enhancement of electrocatalytic water oxidation in alkaline media. *Nat. Energy* **4**, 519–525 (2019).
212. Wang, Y. et al. Current understanding and challenges of solar-driven hydrogen generation using polymeric photocatalysts. *Nat. Energy* **4**, 746–760 (2019).
213. Vyas, V. S., Lau, V. W. & Lotsch, B. V. Soft photocatalysis: organic polymers for solar fuel production. *Chem. Mater.* **28**, 5191–5204 (2016).
214. Banerjee, T., Podjaski, F., Kröger, J., Biswal, B. P. & Lotsch, B. V. Polymer photocatalysts for solar-to-chemical energy conversion. *Nat. Rev. Mater.* **6**, 168–190 (2021).
215. Cao, S., Low, J., Yu, J. & Jaroniec, M. Polymeric photocatalysts based on graphitic carbon nitride. *Adv. Mater.* **27**, 2150–2176 (2015).
216. Ong, W.-J., Tan, L.-L., Ng, Y. H., Yong, S.-T. & Chai, S.-P. Graphitic carbon nitride ($g\text{-}C_3N_4$)-based photocatalysts for artificial photosynthesis and environmental remediation: are we a step closer to achieving sustainability? *Chem. Rev.* **116**, 7159–7329 (2016).
217. Godin, R., Wang, Y., Zwijnenburg, M. A., Tang, J. & Durrant, J. R. Time-resolved spectroscopic investigation of charge trapping in carbon nitrides photocatalysts for hydrogen generation. *J. Am. Chem. Soc.* **139**, 5216–5224 (2017).
218. Walsh, J. J., Jiang, C., Tang, J. & Cowan, A. J. Photochemical CO_2 reduction using structurally controlled $g\text{-}C_3N_4$. *Phys. Chem. Chem. Phys.* **18**, 24825–24829 (2016).
219. Lau, V. W. et al. Rational design of carbon nitride photocatalysts by identification of cyanamide defects as catalytically relevant sites. *Nat. Commun.* **7**, 12165 (2016).
220. Kasap, H. et al. Solar-driven reduction of aqueous protons coupled to selective alcohol oxidation with a carbon nitride–molecular Ni catalyst system. *J. Am. Chem. Soc.* **138**, 9183–9192 (2016).
221. Savoie, B. M. et al. Unequal partnership: asymmetric roles of polymeric donor and fullerene acceptor in generating free charge. *J. Am. Chem. Soc.* **136**, 2876–2884 (2014).
222. Huang, H., Pradhan, B., Hofkens, J., Roeffaers, M. B. J. & Steele, J. A. Solar-driven metal halide perovskite photocatalysis: design, stability, and performance. *ACS Energy Lett.* **5**, 1107–1123 (2020).
223. Singh, S. et al. Hybrid organic–inorganic materials and composites for photoelectrochemical water splitting. *ACS Energy Lett.* **5**, 1487–1497 (2020).
224. Schanze, K. S., Kamat, P. V., Yang, P. & Bisquert, J. Progress in perovskite photocatalysis. *ACS Energy Lett.* **5**, 2602–2604 (2020).
225. Shyamal, S. et al. Facets and defects in perovskite nanocrystals for photocatalytic CO_2 reduction. *J. Phys. Chem. Lett.* **11**, 3608–3614 (2020).
226. Zhu, X., Lin, Y., Sun, Y., Beard, M. C. & Yan, Y. Lead-halide perovskites for photocatalytic α-alkylation of aldehydes. *J. Am. Chem. Soc.* **141**, 733–738 (2019).
227. Cardenas-Morcoso, D. et al. Photocatalytic and photoelectrochemical degradation of organic compounds with all-inorganic metal halide perovskite quantum dots. *J. Phys. Chem. Lett.* **10**, 630–636 (2019).
228. Gualdrón-Reyes, A. F. et al. Unravelling the photocatalytic behavior of all-inorganic mixed halide perovskites: the role of surface chemical states. *ACS Appl. Mater. Interfaces* **12**, 914–924 (2020).
229. Xu, Y.-F. et al. A $CsPbBr_3$ perovskite quantum dot/graphene oxide composite for photocatalytic CO_2 reduction. *J. Am. Chem. Soc.* **139**, 5660–5663 (2017).
230. Park, S., Choi, S., Kim, S. & Nam, K. T. Metal halide perovskites for solar fuel production and photoreactions. *J. Phys. Chem. Lett.* **12**, 8292–8301 (2021).
231. Wang, H. et al. Promoting photocatalytic H_2 evolution on organic–inorganic hybrid perovskite nanocrystals by simultaneous dual-charge transportation modulation. *ACS Energy Lett.* **4**, 40–47 (2019).
232. Kumar, S., Regue, M., Isaacs, M. A., Freeman, E. & Eslava, S. All-inorganic $CsPbBr_3$ nanocrystals: gram-scale mechanochemical synthesis and selective photocatalytic CO_2 reduction to methane. *ACS Appl. Energy Mater.* **3**, 4509–4522 (2020).
233. Huang, Y. T., Kavanagh, S. R., Scanlon, D. O., Walsh, A. & Hoye, R. L. Z. Perovskite-inspired materials for photovoltaics and beyond-from design to devices. *Nanotechnology* **32**, 132004 (2021).
234. Jin, H. et al. It's a trap! On the nature of localised states and charge trapping in lead halide perovskites. *Mater. Horiz.* **7**, 397–410 (2020).
235. Zhu, X.-Y. & Podzorov, V. Charge carriers in hybrid organic–inorganic lead halide perovskites might be protected as large polarons. *J. Phys. Chem. Lett.* **6**, 4758–4761 (2015).
236. Puppin, M. et al. Evidence of large polarons in photoemission band mapping of the perovskite semiconductor $CsPbBr_3$. *Phys. Rev. Lett.* **124**, 206402 (2020).
237. Guzelturk, B. et al. Visualization of dynamic polaronic strain fields in hybrid lead halide perovskites. *Nat. Mater.* **20**, 618–623 (2021).
238. Miyata, K. et al. Large polarons in lead halide perovskites. *Sci. Adv.* **3**, e1701217 (2017).
239. Kabakova, I. V. et al. The effect of ionic composition on acoustic phonon speeds in hybrid perovskites from Brillouin spectroscopy and density functional theory. *J. Mater. Chem. C* **6**, 3861–3868 (2018).
240. Limmer, D. T. & Ginsberg, N. S. Photoinduced phase separation in the lead halides is a polaronic effect. *J. Chem. Phys.* **152**, 230901 (2020).
241. Cui, Y. et al. Metal-free activation of H_2O_2 by $g\text{-}C_3N_4$ under visible light irradiation for the degradation of organic pollutants. *Phys. Chem. Chem. Phys.* **14**, 1455–1462 (2012).
242. Fabian, D. M. et al. Particle suspension reactors and materials for solar-driven water splitting. *Energy Environ. Sci.* **8**, 2825–2850 (2015).
243. Ager, J. W., Shaner, M. R., Walczak, K. A., Sharp, I. D. & Ardo, S. Experimental demonstrations of spontaneous, solar-driven photoelectrochemical water splitting. *Energy Environ. Sci.* **8**, 2811–2824 (2015).
244. Jiang, C., Moniz, S. J. A., Wang, A., Zhang, T. & Tang, J. Photoelectrochemical devices for solar water splitting — materials and challenges. *Chem. Soc. Rev.* **46**, 4645–4660 (2017).
245. Moss, B., Babacan, O., Kafizas, A. & Hankin, A. A review of inorganic photoelectrode developments and reactor scale-up challenges for solar hydrogen production. *Adv. Energy Mater.* **11**, 2003286 (2021).

Acknowledgements

The authors thank L. Harnett for sharing his data and insights on WO_3. E.P. acknowledges support from grant IJC2018-037384-I, funded by MCIN/AEI /10.13039/501100011033. S.S. and J.R.D. acknowledge funding from the European Union's Horizon 2020 Research And Innovation Programme under grant agreements 884444-SUN2CHEM and 732840-A-LEAF. M.S. thanks the UK EPSRC for a Doctoral Prize Fellowship. A.A.B. is a Royal Society University Research Fellow. This work was partially funded by CEX2019-000910-S (MCIN/AEI/10.13039/501100011033), Fundació Cellex, Fundació Mir-Puig and Generalitat de Catalunya through CERCA.

Author contributions

All authors contributed to the writing of the article. E.P. and A.W. also researched the data, discussed the content and edited the article prior to submission.

Competing interests

The authors declare no competing interests.

Peer review information

Nature Reviews Materials thanks Robert Baker, Giulia Galli and the other, anonymous, reviewer(s) for their contribution to the peer review of this work.

Publisher's note

Springer Nature remains neutral with regard to jurisdictional claims in published maps and institutional affiliations.